# Chapter 8

# Field Investigation

Dharmarajika Stupa at Taxila of Pakistan; Taxila,which is close to the capital of Islamabad, is one of the sites of Gandhara civilization in which Greek and Indian Buddhism influences interacted.

## 8.1 Field Investigation on Shear Wave Velocity

The most reliable methods to determine the shear modulus of soil are those conducted in the field. This is because laboratory soil testing of undisturbed soil samples is often subjected to errors due to sample disturbance. Even if the disturbance is minor in advanced technique of sampling, time and expense may be substantial.

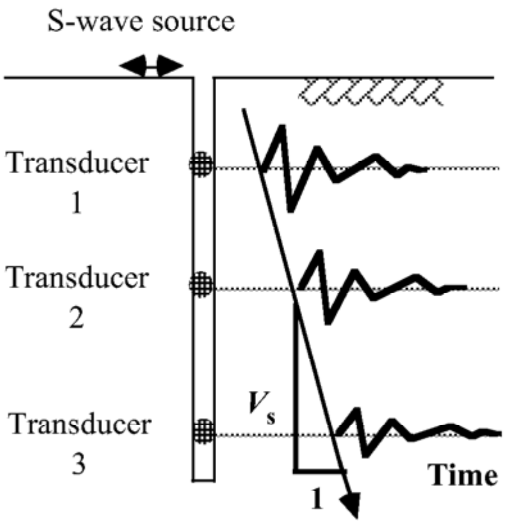

**Fig. 8.1** Principle of downhole survey

In the field, S wave is generated artificially and the wave propagation is recorded. The distance divided by wave travel time is the S-wave velocity, $V_s$ (Fig. 8.1). $G$ is then calculated; $G = \rho V_s^2$. It is important that an artificial source of wave has a limited power and the strain amplitude in the traveling wave is very small (of order of $10^{-6}$ or less). Hence, the obtained $V_s$ corresponds to the modulus at small strain, $G_{max}$ (Fig. 8.2). At this small strain, soil behaves in a nearly elastic manner, and this $G_{max}$ is an elastic property of soil.

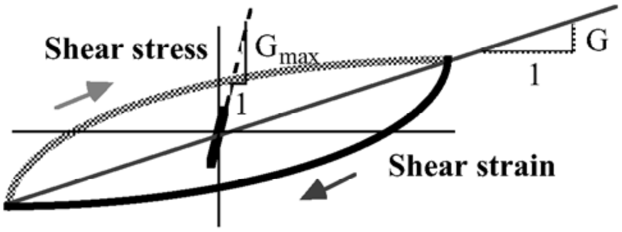

**Fig. 8.2** Variation of shear modulus with strain amplitude

Figure 8.3 illustrates a practice in S wave generation. The dead weight, as produced by the weight of a motor vehicle, should be as large as 9.8 kN (1 ton). Otherwise, the generated wave may not be a good S wave. Hence, the weight of a human body is not sufficient. Note that shear modulus at larger strain amplitude is much smaller than $G_{max}$. For example, 50%, 20%, and <10% of $G_{max}$ (Sect. 10.6).

(Example) Typically, $V_s$ = 100 m/s in soft soil and 300–500 m/s in harder soils. An intact rock mass has $V_s$ = approximately 3,000 m/s. The mass density of soil "$\rho$" is of less variation; $1.4–1.5 \times 1{,}000$ kg/m$^3$ for dry soil and $1.8–2.0 \times 1{,}000$ kg/m$^3$ when water-saturated. Therefore, a water-saturated soft soil has $G_{max} = \rho V_s^2 = 1.8 \times 10^7$ N/m$^2$ = $1.8 \times 10^4$ kN/m$^2$ or 180 kgf/cm$^2$.

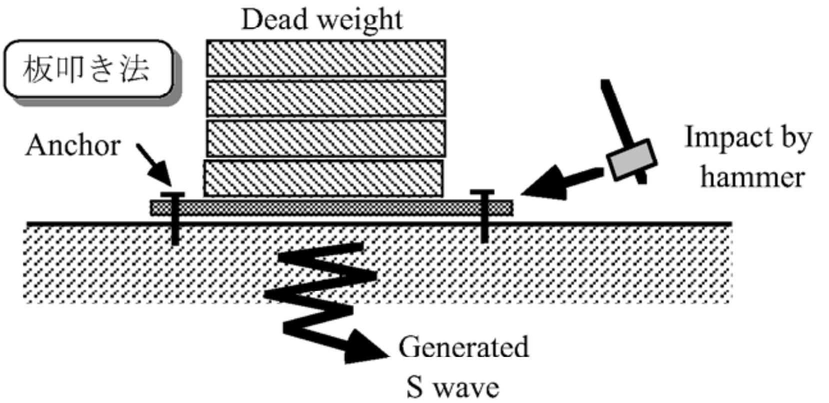

**Fig. 8.3** Practice of downhole PS exploration

In principle, it is possible to determine the P-wave velocity, $V_p$, by similarly generating P wave and monitoring its propagation. This is practiced in geophysical exploration for mining and oil production. However, this P-wave survey is difficult in alluvial soft soil, because the generated P wave propagates through pore water in which $V_p$ is about 1,400 m/s, which is faster than propagation through soil skeleton. Thus, the property of soil skeleton is erased by the behavior of pore water. In contrast, P-wave survey works in harder rock media in which $V_p$ in solid skeleton is faster than 1,500 m/s.

## 8.2 Suspension-Type Downhole Survey

Figure 8.4 reveals the practice of downhole survey data as described in Sect. 8.1. The inclination of travel time lines changes with depth, suggesting the increase of $V_s$ at lower elevations. This figure suggests, however, that $V_s$ is constant over a substantial distance in $z$ directions. Actually, the conventional downhole survey is not so sensible to detect minor change of $V_s$ in $z$ direction. To overcome this problem, a suspension-type (漂遊式) downhole survey was developed (Kitsunezaki, 1978a,b).

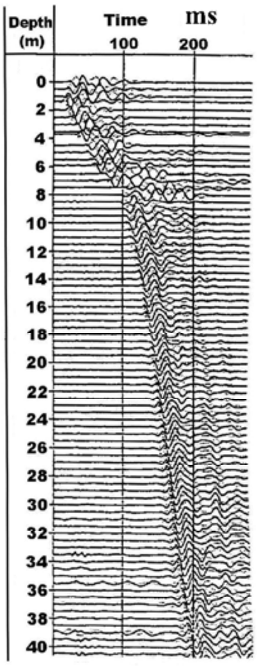

**Fig. 8.4** Conventional downhole survey (ADEP)

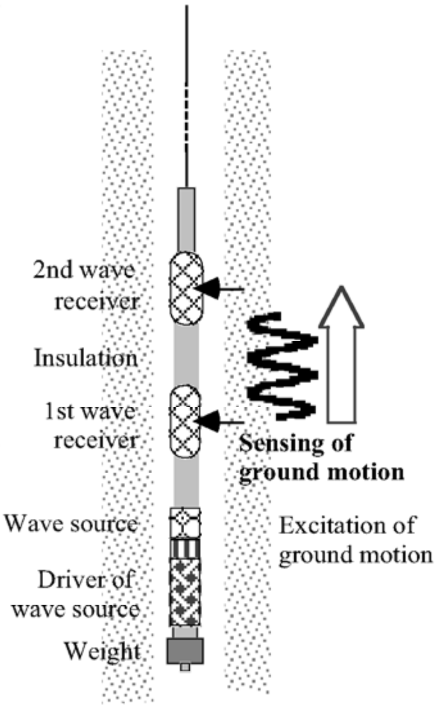

**Fig. 8.5** Suspension-survey in bore hole

A suspension-type device has both the source and two receivers inside a bore-hole equipment (Fig. 8.5). The device measures the local travel time over the interval between two receivers. Therefore, the obtained $V_s$ is local as well over the 1-m interval. The device is placed at the bottom of a bore hole first. Repeating the measurement, the device goes up with a prescribed interval, and finally reaches the ground surface. Figure 8.6 shows a photograph of this equipment.

**Fig. 8.6** Suspension survey equipment on site

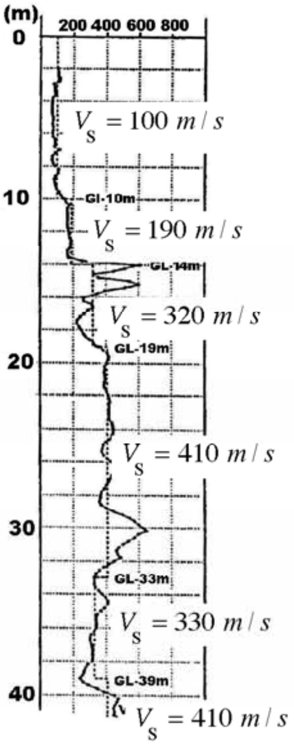

**Fig. 8.7** Suspension-type survey (ADEP)

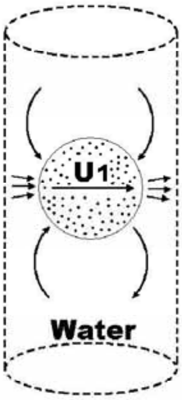

**Fig. 8.8** Detail of wave source in suspension-type instrument (Kitsunezaki, 1978a)

Figure 8.7 illustrates the detailed $V_s$ profile at the same reclaimed island in Tokyo Bay. This was obtained by the suspension-type device, and the detailed variation of $V_s$ with depth and soil type can be seen. It appears to the author that $V_s$ varies continuously with depth.

Figure 8.5 shows the detailed structure of a wave source. This source is submerged in bore-hole water upon survey. A rigid mass installed in the equipment is driven laterally by an electromagnetic mechanism, and creates increased water pressure on one side of a bore-hole wall and reduced pressure on the other side. Accordingly, the ground around the bore hole is sheared laterally and S wave starts to propagate in the vertical direction. The travel time of this wave is monitored by receivers, which are of similar mechanism as the source and detects the lateral movement of bore-hole wall and water in the hole. Note that S wave does not propagate in the bore-hole fluid.

## 🕮 8.3 Cross-Hole Survey

A cross-hole survey requires at least two bore holes. A source is placed in one hole and a receiver is installed in the other, both at the same elevation. The monitored S wave travels in the horizontal direction from the source to the receiver. When a horizontal layer is the case, the measured wave velocity, $V_s$, is the local wave velocity, equivalent to the results of suspension-type survey (Fig. 8.9).

The cross-hole survey is more expensive than the down-hole survey because it needs drilling at least two bore holes. On the other hand, three, four, or more holes can be drilled and wave propagation can be monitored at various distances from the source. This makes it possible to measure not only the travel times and $V_s$ but the decay of wave amplitude with distance. This decay is directly related to the damping ratio of soil.

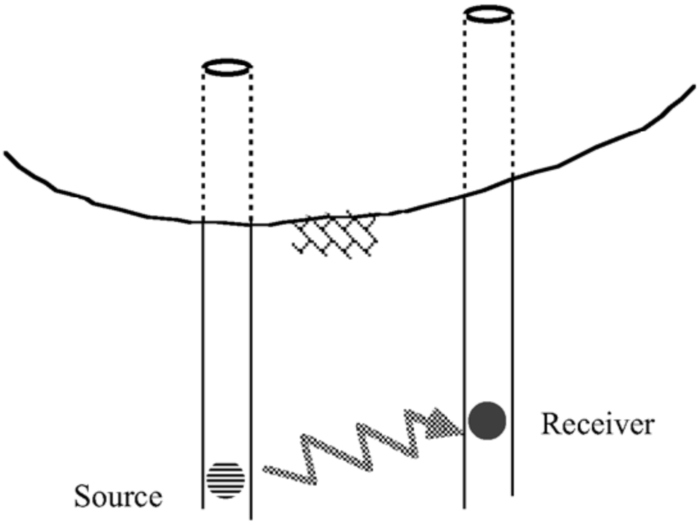

**Fig. 8.9** Cross-hole survey

## 8.4 Correlation Between SPT-*N* and $V_s$ of Alluvial Soils

It is a dream to carry out shear tests in a bore hole, because the obtained stress–strain data would exhibit nonlinear behavior of soil without bad effects of sample disturbance. Although such an attempt has been made by a limited people (for example, Henke and Henke, 1993), its development is not yet satisfactory. Note further that undrained shear is very difficult in bore holes. Hence, the present technology in the field still relies on sounding and measurement of soil resistance against penetration of objects.

Standard penetration test (SPT in Sect. 1.12) is a popular method of subsoil investigation in which a sampler tube is hit into the bottom of a bored hole by an impact made by a hammer of 622.3 N (=63.5 kg) falling 75 cm (Fig. 8.10). The number of impacts needed for 30 cm penetration of a tube is designated by SPT-*N*. Although it is widely used in the world, there are negative discussion about it concerning whether or not its practice is standardized. Despite that, *N* value has been correlated with many engineering soil parameters and the S wave velocity, $V_s$, is not an exception.

**Fig. 8.10** Practice of standard penetration test

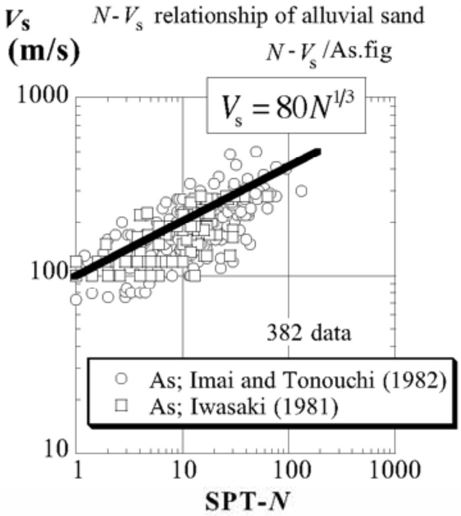

**Fig. 8.11** SPT- $V_s$ correlation for alluvial sandy soils

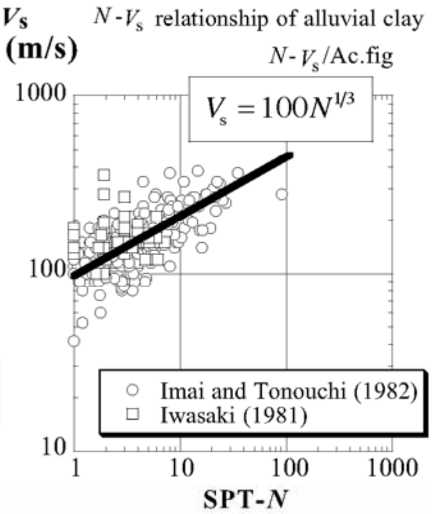

**Fig. 8.12** SPT- $V_s$ correlation for alluvial clayey soils

The penetration of SPT sampler is resisted by soil. When denser and more compacted, soil can produce more resistance and a greater value of *N*. Soils of this type at the same time has a greater shear modulus and $V_s$. Therefore, there is a correlation between *N* and $V_s$.

Many empirical formulae have been proposed by compiling *N* and $V_s$ values, which are measured at the same site and the same depth (Figs. 8.11 and 8.12 for sandy and clayey soils, respectively). Among them, those employed by the Japanese Highway Bridge Design Code appear the easiest to memorize

$$V_s = 80N^{1/3} \text{ (m/s) for sand} \qquad \text{and}$$
$$V_s = 100N^{1/3} \text{ (m/s) for clay,} \qquad (8.1)$$

which are illustrated in Fig. 8.11 and Fig. 8.12. It is not meant here that other formulae are less reliable.

Figure 8.13 shows a similar correlation for $V_s$ of loam (volcanic ash deposit), which is widely seen in Tokyo area. Furthermore, for soft organic soils, $V_s$ = 50–60 m/s appears to be appropriate.

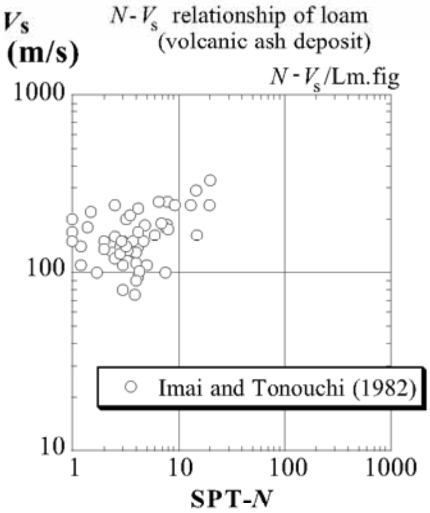

**Fig. 8.13** SPT- $V_s$ correlation for loam (volcanic ash deposits)

One of the problems lying in the correlation is the due scattering of data. Figure 8.11–8.13 demonstrate the data base collected by two literatures. For each type of soil, the observed $V_s$ is roughly between 1/2 and 2 times of the correlation. The scattering occurs due to (1) spatial variation of soil type between SPT and $V_s$ sites, (2) errors in field investigation, and (3) fuzzy nature of soil that does not exactly follow any equation. It is very important that the specified impact energy (622.3 N and 75 cm falling) is precisely produced. Moreover, reasonable maintenance of the SPT equipment is essential.

SPT device collects disturbed sample upon its impact penetration into subsoil at the bottom of a bore hole. Being disturbed (Fig. 1.37), this sample does not suit mechanical testing, but still is useful for physical properties such as particle size distribution and plasticity index. Liquefaction study by means of SPT will be described in Sect. 21.1.

The quaternary geology of alluvial deposits states that alluvial sandy and clayey deposits are underlain by gravels. This gravel layer was formed when the sea water level was still lower than today during the last (Ulm) glacier period. The sea water level achieved the highest level around 6,000 years before present and thereinafter dropped slightly (Fig. 8.14). Consequently, the Japanese alluvial planes consist of such a stratification as illustrated in Fig. 8.15; gravel, clay, and sand from the bottom to the top; overlain by recent surface fills in urban areas.

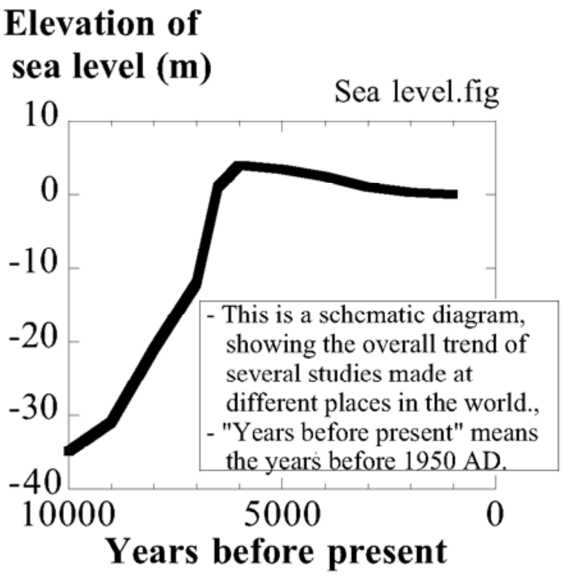

**Fig. 8.14** Sea level rising after last glacier period

The gravelly layer at the bottom of alluvial deposits is frequently employed as the bearing layer of building foundations. Its SPT-$N$ is often greater than 50. Since the sea level change was repeated during the Pleistocene periods, there are more gravelly layers in the Pleistocene strata.

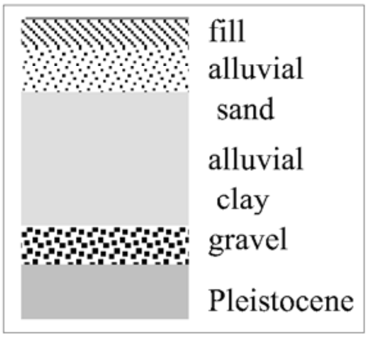

**Fig. 8.15** Schematic stratification of alluvial plane in Japan

Figure 8.16 indicates the relationship between SPT-$N$ and $V_s$ of both alluvial (Holocene) and Pleistocene gravelly deposits. Generally, the Pleistocene gravel has greater penetration resistances and $V_s$ values than the younger alluvial (Holocene) materials. However, the correlation between SPT-$N$ and $V_s$ is similar in those two gravels.

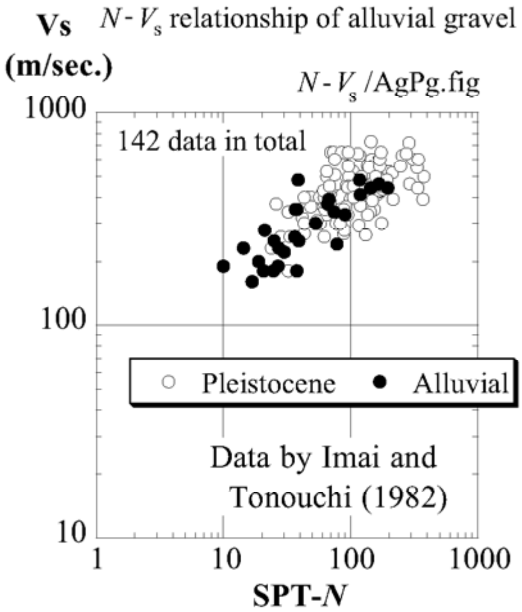

**Fig. 8.16** SPT-$V_s$ correlation of Pleistocene and Holocene gravels

Figure 8.16 gives an impression that SPT-$N$ > 300 was obtained by repeating the impact procedure as many as 300 times. It may not be true. It is a common practice that the penetration procedure is terminated after some number of blows when the achieved penetration is far less than the required 30 cm. If this is the case, SPT-$N$ is obtained by exptrapolation. For example,

$$(\mathrm{SPT}-N)=(\text{Number of blows})\times\frac{30\ cm}{\text{Achieved penetration}}.$$

## 8.6 Correlation Between SPT-*N* and $V_s$ of Pleistocene Soils

For construction of heavy structures, investigation on Pleistocene deposits is important. Figure 8.17 and Figure 8.18 plot SPT-*N* versus S-wave-velocity ($V_s$) relationships on Pleistocene sands and clays. Comparison is also made with similar data on alluvial soils which were presented in Sect. 8.4.

Pleistocene sands and clays certainly have greater SPT-*N* and S wave velocity. It is interesting that the average correlations for Pleistocene materials are consistent with those for alluvial soils.

Since the measured $V_s$ values are still less than 1,000 m/s, it is reasonable to state that Pleistocene soils are softer than sedimentary rocks, which, if free of weathering and joints, have $V_s$ of 1–3 km/sec.

Some people prefer to use a terminology of "diluvial" in place of Pleistocene. The meaning of this word is related to flooding. Since the gravelly deposits of the last glacier period used to be considered to be a product of flooding, this word has been used. Recently, quaternary geologists consider that the deposits during the glacier period are not necessarily a product of flooding, and state that "diluvial" is not a relevant terminology. Hence, the present text uses the word of Pleistocene. Moreover, "Holocene" is an alternative word for "alluvial" for more recent deposits. There is not, however, a situation against the use of "alluvial."

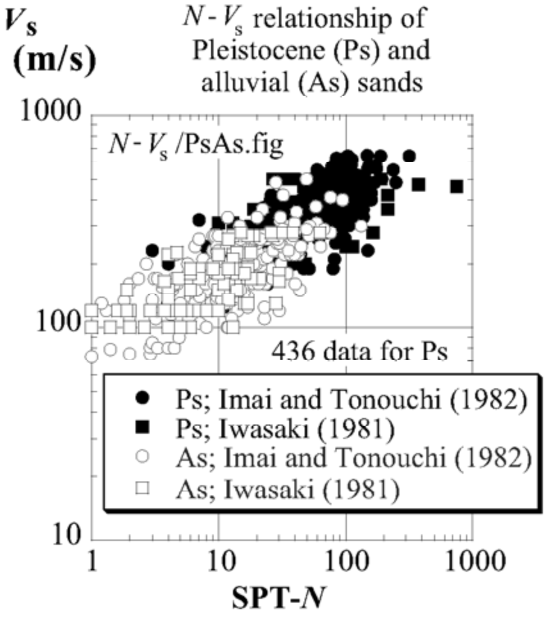

**Fig. 8.17** SPT-$V_s$ correlation of Pleistocene sands as compared with alluvial sands

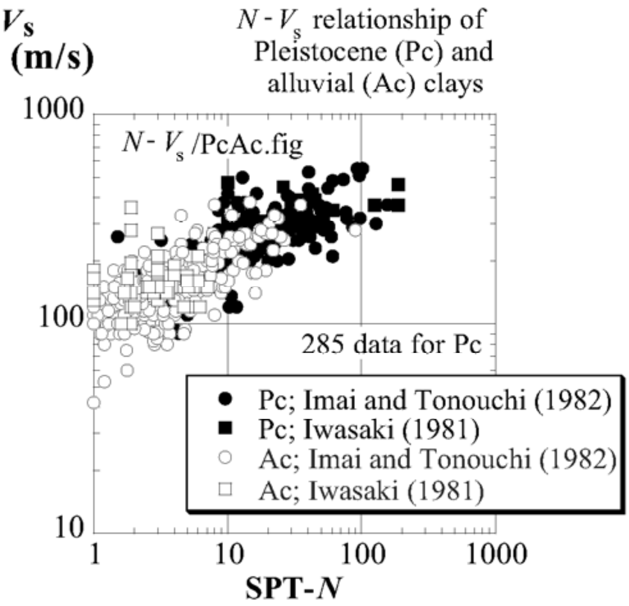

**Fig. 8.18** SPT-$V_s$ correlation of Pleistocene clays as compared with allluvial clays

## 8.7 Seismic Refraction Method for Subsurface Exploration

One of the famous applications of wave propagation to the subsurface investigation is the seismic refraction method (屈折法地盤探査). In this method, the wave propagation velocity, $V_p$ or $V_s$, is measured and the shear modulus of soil at small strain amplitude, $G_{max}$, is determined by using $V_s$

$$G_{max} = \rho V_s^2. \qquad (8.2)$$

Note that $\rho$ is the mass density of soil and can be safely assessed to lie between 1.5–2.0 t/m$^3$, depending on density and water content. In practice, P wave is more often investigated than S wave.

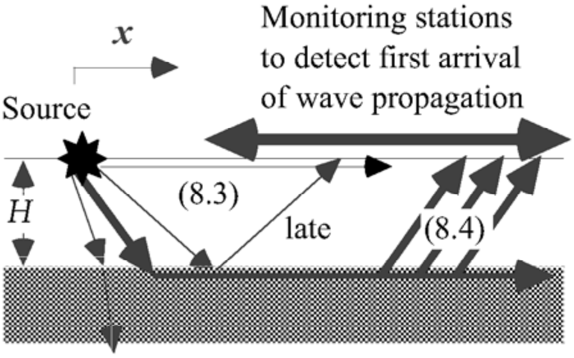

**Fig. 8.19** Basic principle of seismic refraction method in horizontally layered deposits

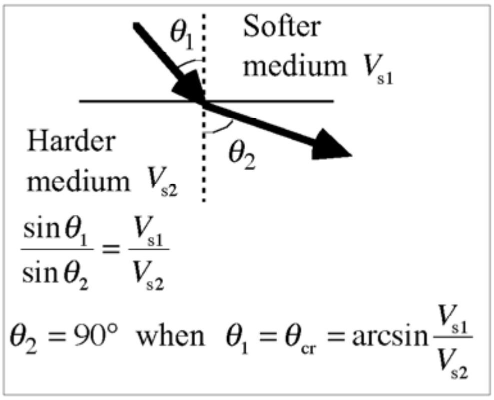

**Fig. 8.20** Snell's law of wave refraction at interface of two different media

Figure 8.19 illustrates the principle of the method. Wave is generated by a source at the surface and propagates into the ground as well as along the surface.

1. Near the source, the first arrival of ground vibration is associated with the surface propagation. The travel time, $T$, from the source to the stations are given by

   $$T = x/V_{s1}, \qquad (8.3)$$

   where $x$ is the distance from the source and $V_{s1}$ the wave velocity in the surface soft medium. Those waves reflected (反射) at the bottom of the layer arrive later.
2. Beyond some distance, in contrast, the wave propagation along the harder underlying deposit arrives first. Its travel time is given by

   $$T = \frac{2H}{\cos\theta_{cr} V_{s1}} + \frac{x - 2H\tan\theta_{cr}}{V_{s2}}. \qquad (8.4)$$

   This wave propagation is achieved by the generated wave whose incident angle at the layer interface satisfies a special requirement of $\theta_1 = \theta_{cr}$ from the Snell's law (Fig. 8.20).
3. In (8.3) and (8.4), $V_{s1}$, $V_{s2}$, and $H$ are unknown, while $\theta_{cr}$ is a function of $V_{s1}$ and $V_{s2}$ (Fig. 8.20).
4. Figure 8.21 is a schematic relationship between $x$ and the observed travel time, $T$. When there are two layers, the data points are approximated by a bilinear relationship.
5. The slopes of the bilinear relationship give the value of $V_{s1}$ and $V_{s2}$ as well as $\theta_{cr} = \arcsin(V_{s1}/V_{s2})$. The layer thickness, $H$, is determined from the observed intersection of two lines, $x_{cr}$, which is derived by equating (8.3) and (8.4)

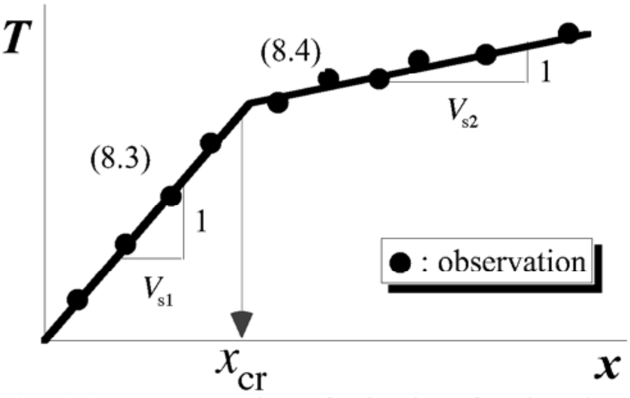

**Fig. 8.21** Interpretation of seismic refraction data on horizontally deposited two layers

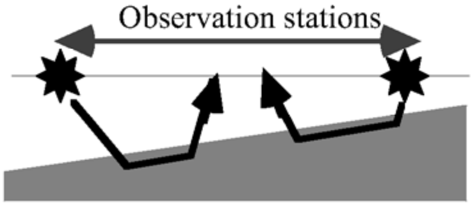

**Fig. 8.22** Seismic refraction survey as provision for inclined layer boundary

$$x_{\mathrm{cr}} = 2H\sqrt{\frac{V_{\mathrm{s2}} + V_{\mathrm{s1}}}{V_{\mathrm{s2}} - V_{\mathrm{s1}}}}. \qquad (8.5)$$

Note that this method works when the underlying layer has a greater stiffness than the surface soil. Furthermore, it is often the case that the layer interface is inclined (Fig. 8.22). Hence, the seismic refraction survey is repeated in positive and negative $x$ directions and the inclination angle is assessed as well.

## 8.8 Stacking Technique to Remove Noise from Signal

It is not uncommon that a geophysical survey such as seismic refraction is disturbed by environmental noises, which include typically traffic-induced vibrations in urban areas. Electromagnetic record of geophysical survey is disturbed as well by such a noise as ground electric current produced by trains and the existence of buried metal pipes.

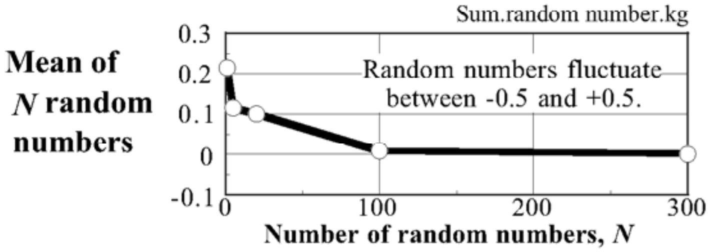

**Fig. 8.23** Mean value of random numbers approaching zero as the total number of data increases

To remove noise and obtain a meaningful signal, a technique called stacking is useful. Since the noise is more or less of a randomly positive / negative nature, the stacking technique is based on the fact that the mean value of random numbers converges to zero when the total number of data is large as demonstrated in Fig. 8.23

$$\frac{1}{N}\sum_{i=1}^{N}(\text{random number})_i \to 0 \quad \text{when } N \to \text{infinity}. \tag{8.6}$$

Figure 8.24 is a time history of a signal that is intended to be recorded. Being masked by a significant intensity of a noise in Fig. 8.25, the observed signal in Fig. 8.26 is totally different from the desired one in Fig. 8.24.

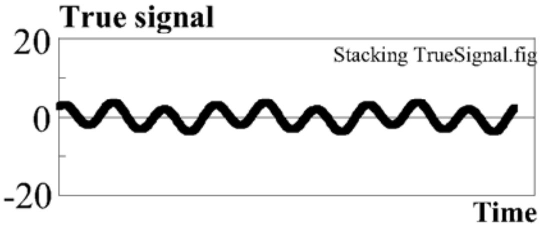

**Fig. 8.24** True time history of record

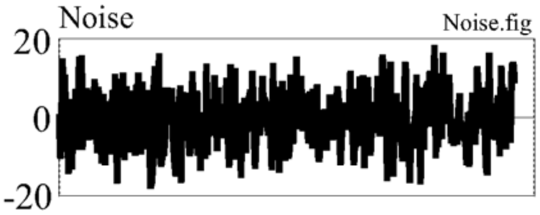

**Fig. 8.25** Intensity of noise

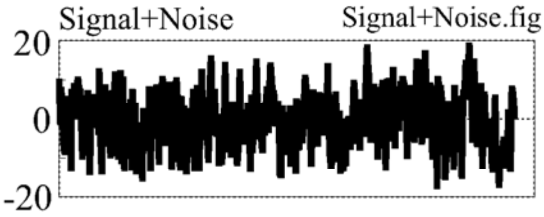

**Fig. 8.26** Superposition of signal and noise in actual observation

To overcome this problem by the stacking technique, monitoring is repeated *K* times, records are added (stacked) together, and the average is calculated

$$\text{Stacked record} = \frac{1}{K}\sum_{j=1}^{K}(\text{Recorded signal})_j \ . \tag{8.7}$$

Figure 8.27–8.29 illustrate the results of stacking after numerically repeating the monitoring 5, 20, and 100 times, respectively. The signal–noise ratio (*S*/*N*) was improved as the number of stacking increased. Consequently, the time history after 100 times stacking (Fig. 8.29) is more meaningful than a single shot of recording in Fig. 8.26. In practice, the stacking procedure is often conducted by adding data in the frequency–intensity diagram in place of the time domain as illustrated above.

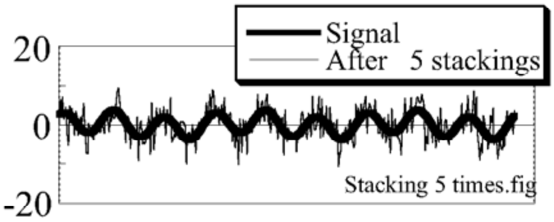

**Fig. 8.27** Record after 5 times stacking

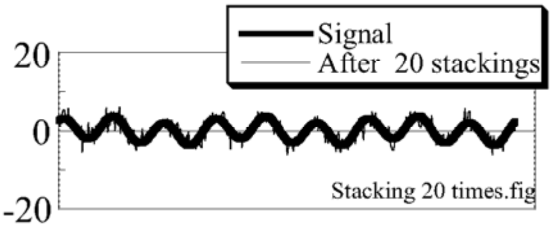

**Fig. 8.28** Record after 20 times stacking

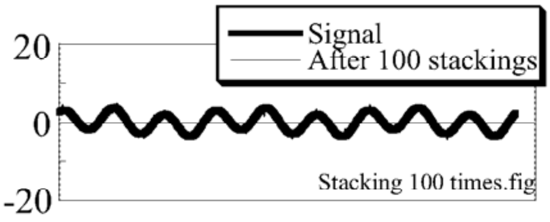

**Fig. 8.29** Record after 100 times stacking

The stacking as described above is carried out in the time domain: the added records stand for variation with time. One of the difficulties in the stacking in the time domain is the determination of the common zero time in many records. If this determination is difficult, an alternative choice is found in stacking in the frequency domain (Miyashita, 2006). First, the recorded signals, $u_j(t)$, are converted to absolute values, $|u_j(t)|$. This procedure converts negative signals to positive ones (Fig. 8.30), making the frequency doubled (horizontal axis of Fig. 8.31). Then the Fourier transformation (Sect. 9.12) is conducted on the absolute values

$$|u_j(t = k\Delta t)| = \sum_{m=0}^{N/2} C_{j,m} \exp\left(\frac{2\pi mk}{N} i\right), \qquad (8.8)$$

in which $k$ = 0, 1, 2,⋯, $N$/2 and $N$ is the number of the entire data. Thus, $C_{j,m}$ stands for the intensity of records at different frequencies.

The same procedure is repeated for many data sets, $j$=1, 2,⋯. Figure 8.31 illustrates the schematic variation of Fourier amplitudes, $|C_{j,m}|$. Note that $|C_{j,m}|$ is more or less similar in the range of true signal, because the signal is equally included in all the sets of data ($j$=1,2,3⋯). In contrast, $|C_{j,m}|$ in the high frequency range, which stands for noise, is random. Thus, after stacking (adding) and averaging, the peak value can be detected more clearly. The predominant frequency (resonance frequency in a structural response) can be determined easily. Since the absolute values of $|C_{j,m}|$ are employed in the analysis, information on phase of signal is lost.

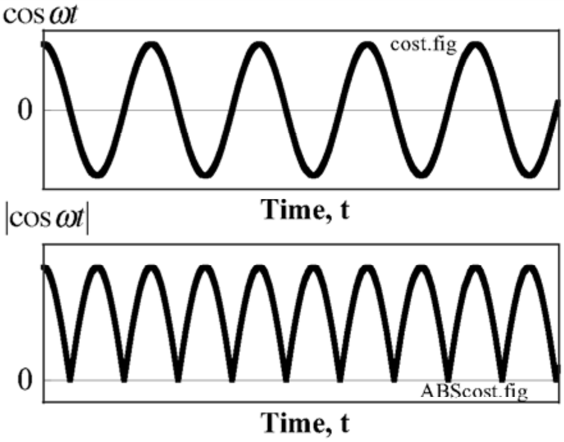

**Fig. 8.30** Time history which is squared to erase negative parts

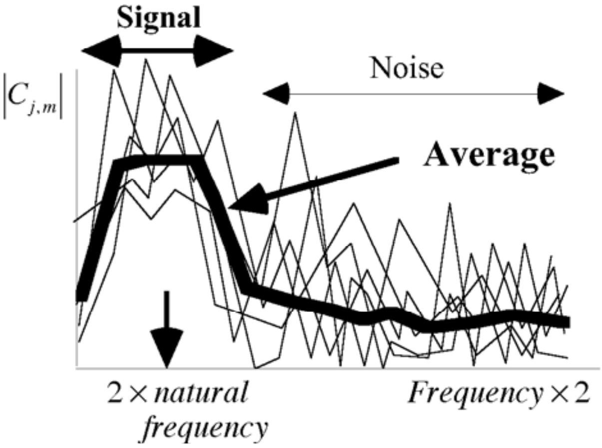

**Fig. 8.31** Stacking in frequency domain

## 8.9 Swedish Weight Sounding

**Fig. 8.32** Rotating Swedish weight sounding device (100 kgf=0.98 kN)

Swedish weight sounding is a portable method of ground investigation and is convenient for earthquake damage investigation when a motor vehicle and electricity are not available. This equipment consists of a screw point at the tip, steel rods of 1 m in length, dead weight of 0.98 kN (100 kgf), and a top handle.

Figure 8.32 shows engineers who are investigating the subsoil condition at a site of liquefaction of silty sand after the 2000 Tottori-Ken Seibu earthquake, Japan. Since no bore-hole drilling is necessary, the investigation is quick and cheap. The added dead weight of $W_{sw}$ = *0.98 kN* makes penetration easy. The equipment is rotated, and the number of half rotations (180-degree rotations) needed for 1m penetration is counted and called $N_{sw}$. Certainly, the harder soil creates the greater value of $N_{sw}$. When soil is extremely soft, penetration occurs without any rotation; the dead weight of the equipment and the additional weight at the top ($W_{sw} \leq 100$ kgf = 0.98 kN) are sufficient to cause self-weight penetration.

The results at the site of Fig. 8.32 is presented in Fig. 8.33. The value of $N_{sw}$ is very low in the young reclaimed sand, which came from a dredging project of a nearby harbor.

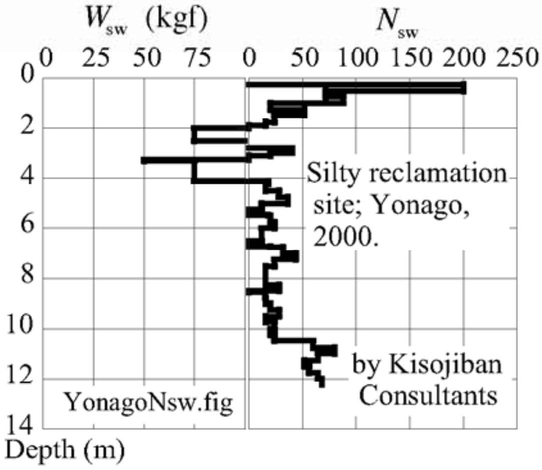

**Fig. 8.33** $N_{sw}$ profile at the site of Fig. 8.32

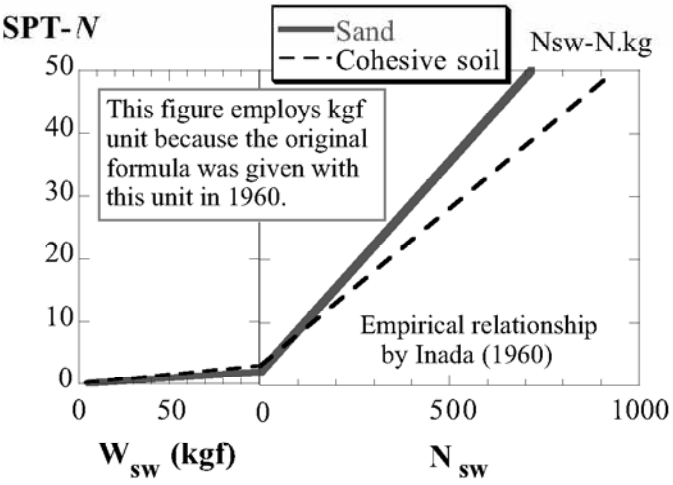

**Fig. 8.34** Empirical correlations between $N_{sw}$ and SPT-*N* (Inada, 1960)

Inada (1960) proposed empirical correlations between $N_{sw}$ and SPT-*N* (Fig. 8.34);

For sand, $N = 0.02 W_{sw}(\text{kgf})$ and $N = 2 + 0.067 N_{sw}$

for cohesive soil, $N = 0.03 W_{sw}(\text{kgf})$ and $N = 3 + 0.05 N_{sw}$.

He stated that the correlation depends upon the types of soil and other factors and that a possible range of error is $\Delta N = \pm 1.5 - 4$ for sandy soils and ±3 for cohesive materials. Thus, the soil profile in Fig. 8.33 has an equivalent *N* less than 5.

When an extremely soft soil is encountered by this device, the whole machine drops suddenly into the ground. In such a situation, caution is necessary not to have your foot injured by the heavy weight of the equipment. Kisojiban Consultants Co. Ltd. of Tokyo developed a portable version of Swedish weight sounding machine in which the 100 kgf weight is produced by sand, which is collected at sites (Fig. 5.45). Thus, there is no need to carry the heavy iron weight.

## 8.10 Microtremor

Microtremor (常時微動) is a very weak ground motion that is recorded at the ground surface. It is produced by a variety of excitation such as wind, traffics, sea wave, etc. It has been expected that the period of microtremor has a reasonable relationship with the nature of local soil deposit and dynamic characteristics of subsoil.

Kanai and Tanaka (1961) proposed to classify the type of ground on the basis of microtremor records. In their first proposal (Fig. 8.35), the subsoil classification was made on the basis of the period of motion. Moreover, they proposed the second classification on the basis of amplification of motion. Since the microtremor amplitude was varied by ambient noise in the daytime and night, they used the mean value of large amplitudes that often appear.

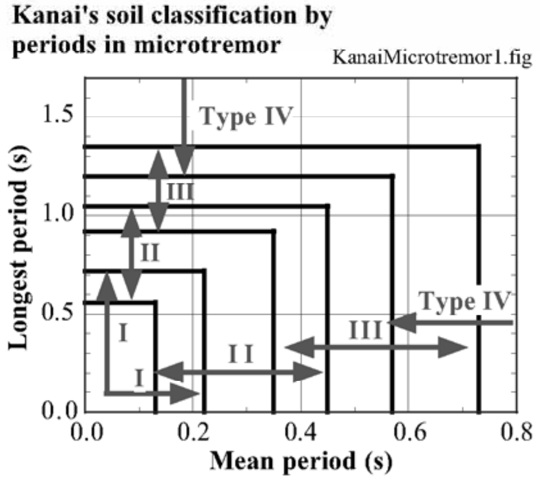

**Fig. 8.35** Subsoil classification based on period of microtremor (drawn after Kanai and Tanaka, 1961).

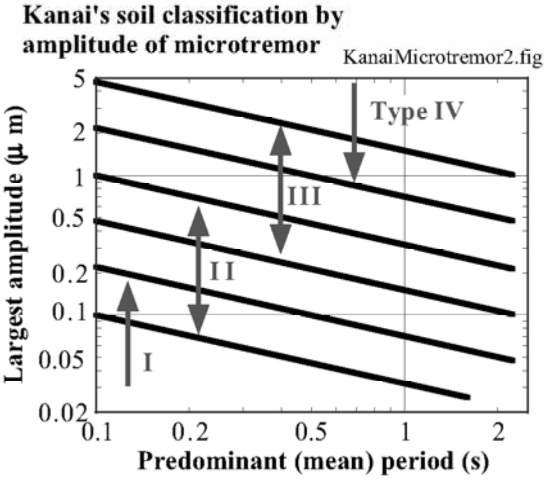

**Fig. 8.36** Subsoil classification based on period of microtremor (drawn after Kanai and Tanaka, 1961)

Kanai and Tanaka (1961) showed a good correlation between the subsoil classification (combination of two classifications in Figs 8.35 and 8.36) and damage rate of Japanese traditional wooden houses (1944 Tonankai earthquake, Kikugawa River District), see Fig. 8.37. This seems to be one of the earliest attempts of seismic microzonation which is based on local soil conditions.

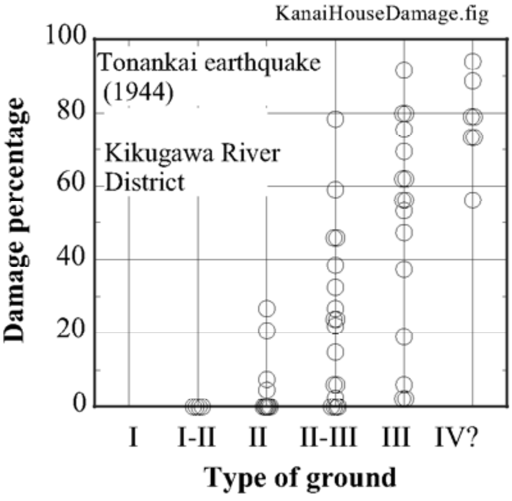

**Fig. 8.37** Correlation between Kanai's subsoil classification and damage rate in Japanese traditional houses

Nakamura (2000) described his idea on use of microtremor records for more detailed classification of subsoil conditions. To the author´s understanding, Nakamura´s *H*/*V* spectrum method postulates that the shape of the Fourier spectrum (Sects. 6.4 and 9.11) of the vertical motion is identical between the base rock and the ground surface (Fig. 8.38), while the horizontal motion is subject to significant amplification (Sect. 6.7). Hence the amplification ratio, AMP(*E*+*F*), is evaluated briefly by the following formula

$$\mathrm{AMP}(E+F) \equiv \frac{\text{Spectrum of surface horizontal motion}}{\text{Spectrum of horizontal motion at baserock}} \propto \frac{\text{Spectrum of surface horizontal motion}}{\text{Spectrum of surface vertical motion}}. \qquad (8.9)$$

This equation enables to determine the natural frequency of the surface deposit by simply using the surface records of microtremor. Thus, it is expected that the surface deposit is classified from the viewpoint of earthquake response.

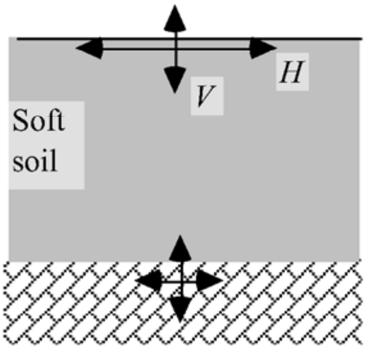

**Fig. 8.38** Principle of $H/V$ spectrum method

The author measured the microtremor at several places around the Kushiro Swamp of Hokkaido (Fig. 8.39). The amplitude of the measured records increased as the point of measurement proceeded towards the center of the swamp (Fig. 8.40). Moreover, The H/V study of the measured records showed that the predominant period of microtremor became longer in the inner part of the swamp (Fig. 8.41). Thus, the above-mentioned expectation seems reasonable. This measurement was conducted from 4 AM to 6 AM after which construction works started and microtremor signal was erased by noise.

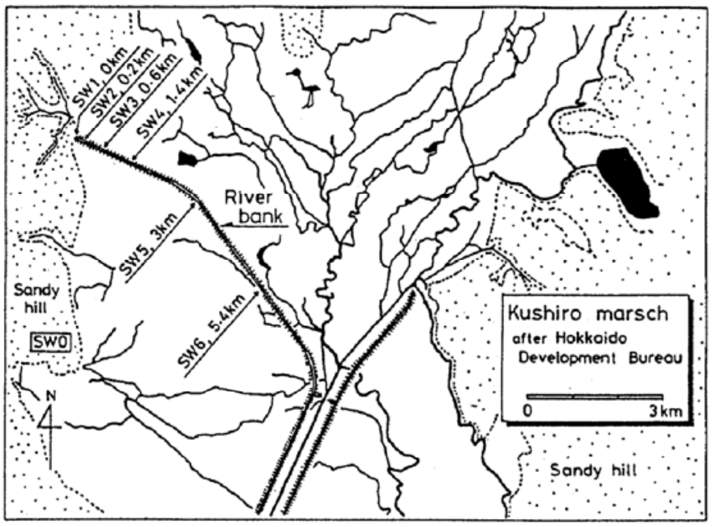

**Fig. 8.39** Variation of predominant period with increasing thickness of peaty subsoil

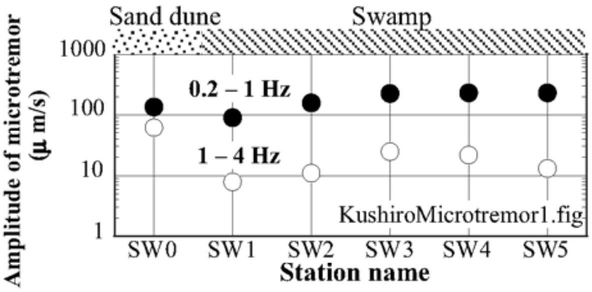

**Fig. 8.40** Variation of microtremor amplitude in Kushiro Swamp

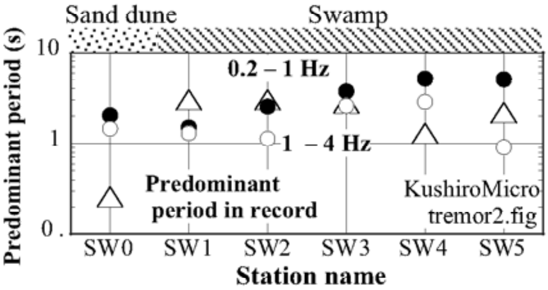

**Fig. 8.41** Variation of predominant and $H/V$ period in Kushiro Swamp

Because of its simplicity, Nakamura´s method is widely used and many good performances have been reported. However, it is yet to be known whether or not the shape of the Fourier spectrum of the vertical motion is unchanged between the bottom and the surface. Thus, the use of this method needs care. Note that the strain level caused by microtremor is extremely small (for example less that $10^{-8}$) and the concerned soil rigidity is $G_{\max}$. Soil behavior during strong shaking is associated with $G$, which is smaller than $G_{\max}$ due to stress–strain nonlinearity (Chap. 10).

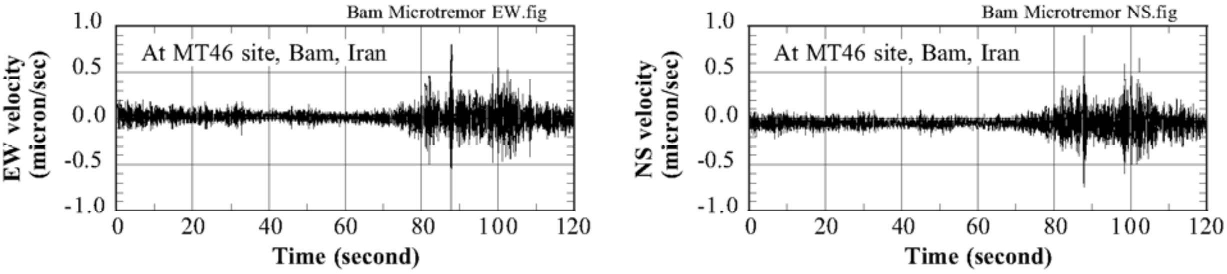

**Fig. 8.42** Example of microtremor records (Motamed et al. 2007)

The following section demonstrates one successful use of the Nakamura´s method that was conducted in the city of Bam after a devastating earthquake in 2003 (Motamed et al. 2006). Figure 8.42 indicates the recording of microtremor. Care is certainly needed to avoid disturbance in the signal due to ambient heavy traffic or construction noise. Microtremor is usually recorded in terms of velocity. Figure 8.42

illustrates an example; see the very small intensity of motion and the associating soil strain. The spectral components of the recorded motions were obtained by Fourier Transformation Technique and then the ratio of horizontal spectrum over the vertical one was obtained. This ratio is called the *H*/*V* spectrum and has no dimension. The obtained *H*/*V* spectrum in Fig. 8.43 exhibits the greatest amplification at around 10 Hz. This frequency is considered to be the natural (resonance) frequency under small shear strain and is closely related with the nature of subsoil.

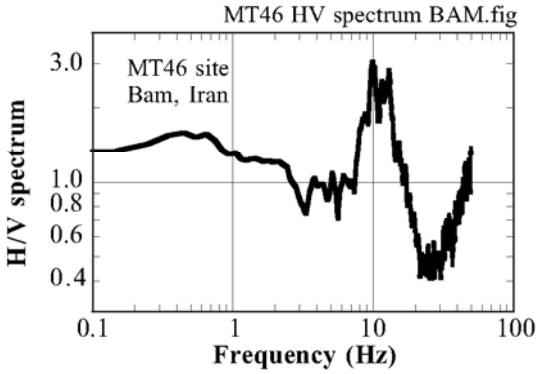

**Fig. 8.43** Example of *H*/*V* spectrum (Motamed et al., 2007)

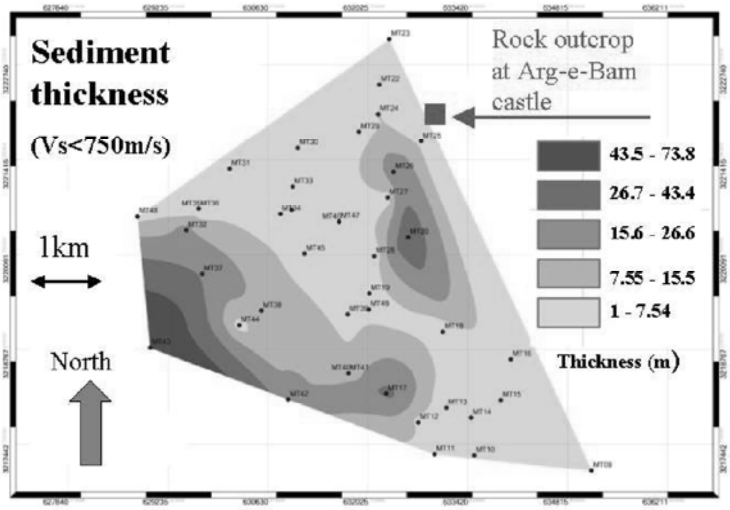

**Fig. 8.45** Assessed depth of baserock in Bam City (Motamed et al., 2007)

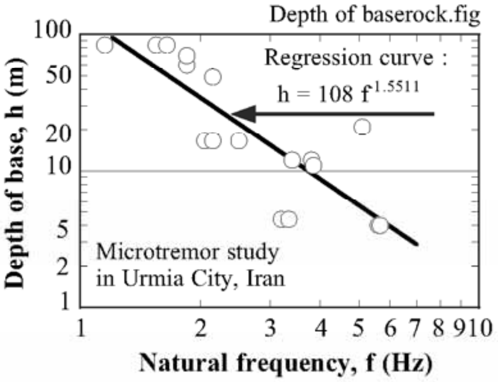

**Fig. 8.44** Empirical correlation between assessed natural frequency and depth of baserock in Urmia City Ghalandarzadeh., 2006)

**Fig. 8.46** Ongoing monitoring of microtremor in Kushiro City

Fig. 8.44 indicates an example of empirical correlation that was obtained in Urmia City of Iran between the obtained natural frequency and the depth of baserock as detected by nearby boring profiles. Note that the baserock is defined by S-wave velocity exceeding 750 m/s as specified by the Iranian code for earthquake-resistant design of buildings. Since there is a reasonable correlation in this figure, it was applied to the natural frequency in Bam city and the thickness of surface soil (= depth of baserock) was determined as illustrated in Fig. 8.45.

Microtremor can be recorded by a convenient portable instruments. However, the recording is easily disturbed by such an environmental noise as caused by traffics and construction works. It is therefore desirable to conduct it during quiet night times (Fig. 8.46).

## 8.11 Subsurface Exploration by Surface Wave Records

The use of microtremor as described in Sect. 8.10 is good because of its simplicity. It is important as well that no drilling of bore hole is required. It is, however, difficult to assess more detailed stratification of subsoils as usually required by geotechnical engineering. In contrast, the recent developments of advanced interpretation of microtremors have made it possible to draw such a stratification.

The new methodology is called SASW (spectral analysis of surface waves) and considers the measured ground vibration as Rayleigh wave (Stokoe et al. 1994), which is a wave that travels along the ground surface (Sect. 4.7). Figure 4.14 illustrated that the propagation velocity of Rayleigh wave is nearly equal to the S-wave velocity ($V_s = \sqrt{G/\rho}$).

Tokimatsu et al. (1991, 1992a,b) classified SASW into passive and active types. The passive type monitors natural microtremors whose source is unknown and the direction of propagation is unknown either. Hence, transducers (geophones) have to be deployed on the ground surface in a two-dimensional manner. On the contrary, the active survey hits the ground surface and monitors the wave propagation along a known path. Thus, the transducers are placed along the same path in a one-dimensional manner. They also stated that the natural microtremor is more advantageous because components of longer wave length are included, which enable us to study soils at deeper elevations.

Figure 8.47 illustrates a situation in which motion "u" propagates in the $x$–$y$ plane. The solution for this wave propagation is generally given by

$$u = F\left(\omega t - k_x x - k_y y\right), \tag{8.10}$$

where $\omega$ stands for the circular frequency, while $k_x$ and $k_y$ are two-dimensional wave numbers. Since the direction of wave propagation ($\eta$) is not known, the values of those wave numbers are unknown.

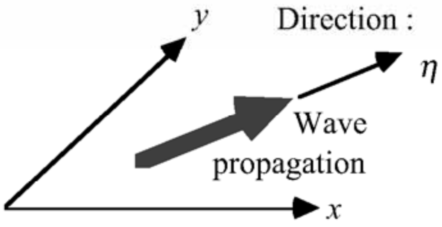

**Fig. 8.47** Propagation of wave in $x$–$y$ horizontal plane

The subsurface exploration technology deploys many transducers at the ground surface and determines the direction of wave propagation. Hence,

$$u = F(\omega t - k\eta), \tag{8.11}$$

in which $k(\omega)$ is the wave number in the direction of wave propagation and varies with $\omega$ when subsoil consists of many layers. The wave length, $L$, is then given by

$$L(\omega) = 2\pi/k,$$

which is a function of $\omega$ as well.

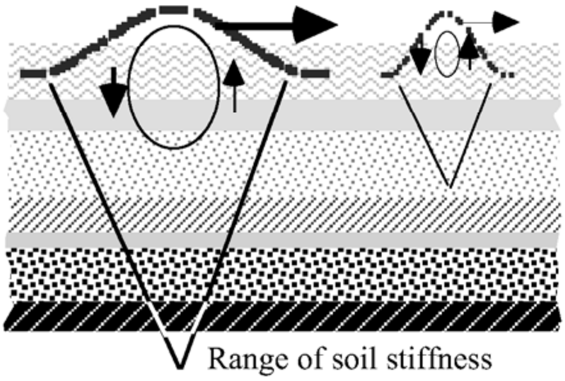

**Fig. 8.48** Effects of wave length on propagation velocity of Rayleigh wave

The analysis of records from transducers makes it possible to determine the wave propagation velocities at many circular frequencies

Velocity of Rayleigh wave propagation $V_R(\omega) \approx V_s$ and $V_R(\omega) = \omega/k$. (8.12)

Consequently, $k$ and wave length, $L$, are determined as

$$k = \omega / V_R \quad \text{and} \quad L = 2\pi V_R / \omega . \tag{8.13}$$

Thus, a correlation between $L$ and $V_s = \sqrt{G/\rho} \approx V_R$ is obtained. Usually, $V_R$ increases as the wave length, $L$, becomes longer, because Rayleigh waves of longer wave length involve effects of deeper and stiffer (greater $G$) soils (Fig. 8.48).

What has to be done is a back calculation of subsoil profile (variation of $V_s$ with depth) that gives the best fitting between analytical and observed $L - V_s$ relationships. Tokimatsu et al. (1991) introduced a mathematical procedure for this procedure. However, the most primitive method for this is to consider that the obtained $V_R \approx \sqrt{G/\rho}$ occurs at $L / 2$. Note that the obtained G is the modulus at small strain, and nonlinearity is out of scope.

## List of References in Chapter 8

Ghalandarzadeh, A. (2006) Personal communication on comprehensive subsoil investigation in Urmia City, Iran.

Henke, W. and Henke, R. (1993) Laboratory evaluation of in situ geotechnical torsional cylindrical impulse shear test for earthquake resistant design, Bull. Seismol. Soc. Am., Vol. 83, No. 1, pp. 245–263.

Imai, T. and Tonouchi, K. (1982) Correlation of *N* value with S-wave velocity and shear modulus, Proc. 2nd Eur. Symp. Penetration Testing, pp. 67–72.

Inada, M. (1960) Interpretation of Swedish weight sounding, Tsuchi-to-Kiso, Japan. Soc. Soil Mech. and Found. Eng. (present Japan. Geotech. Soc.) Vol. 8, No. 1, pp. 13–18 (in Japanese).

Iwasaki, T. (1981) Seismic design of highway bridges, Ph.D. Thesis, Kyushu University (in Japanese).

Kanai, K. and Tanaka, T. (1961) On Microtremors. VIII, Bull. Earthq. Res. Inst., University of Tokyo. Vol. 39, pp. 97 –114.

Kitsunezaki, C. (1978a) Indirect excitation type source for shear wave logging (1), Geophysical Exploration, Vol. 31, No. 6, pp. 329–337.

Kitsunezaki, C. (1978b) Indirect excitation type source for shear wave logging (2), Geophysical Exploration, Vol. 31, No. 6, pp. 338–346.

Miyashita, T. (2006) Personal communication.

Motamed, R., Ghalandarzadeh, A. and Towhata, I. (2007) Seismic microzonation and damage assessment of Bam City, southeast of Iran, J. Earthq. Eng., Vol. 11, No. 1, pp. 110–132.

Nakamura, Y. (2000) Clear identification of fundamental idea of Nakamura's technique and its applications, Proc. 12th World Conf. Earthq. Eng., Auckland, Paper number = 2656 in CD ROM proceedings.

Stokoe, K.H., II, Wright, S.G., Bay, J.A. and Roësset, J.M. (1994) Characterization of geotechnical sites by SASW method, R.D. Woods, eds., Geophysical Characterization of Sites, Publication of Technical Committee 10, Int. Soc. Soil Mech. Found. Eng., Oxford & IBH Publishers, pp. 15–25.

Tokimatsu, K., Kuwayama, S., Tamura, S. and Miyadera, Y. (1991) $V_s$ determination from steady state Rayleigh wave method, Soils and Foundations, Vol. 31, No. 2, pp. 153–163.

Tokimatsu, K., Tamura, S. and Kojima, H. (1992a) Effects of multiple modes on Rayleigh wave dispersion characteristics, J. Geotech. Eng., ASCE, Vol. 118, No. 10, pp. 1529–1543.

Tokimatsu, K., Shinzawa, K. and Kuwayama, S. (1992b) Use of short-period microtremors for $V_s$ profiling, J. Geotech. Eng., ASCE, Vol. 118, No. 10, pp. 1544–1558.

# Chapter 9

# Dynamic Response of Complex-Modulus Model

Tomb mound of the fifth emperor of Han Dynasty, Xi'an, China.
This powerful monarch expanded his territory to Korea, Vietnam, and Central Asia. Even today, his strong spirit still punishes those who do not respect his tomb.

## 9.1 Complex Stress-Strain Modeling

The stress–strain relationship in complex numbers is given by

$$\tau^* = G(1+2ih)\gamma^*$$

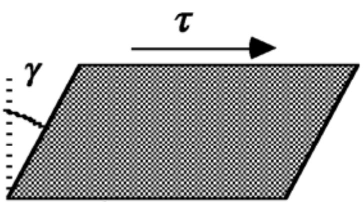

**Fig. 9.1** Stress and strain in simple shear

in which $G$ and $h$ are real numbers, while $i=\sqrt{-1}$ (Fig. 9.1). $G$ is the elastic shear modulus and $h$ is called the damping ratio. When the complex strain varies with time in a harmonic manner,

$$\gamma^* = \gamma_o \exp(i\omega t) = \gamma_o(\cos\omega t + i\,\sin\omega t)$$

the complex stress varies in a harmonic manner as well

$$\tau^* = G\gamma_o(\cos\omega t + i\,\sin\omega t)(1+2ih) = G\gamma_o\{(\cos\omega t - 2h\,\sin\omega t) + i(\sin\omega t + 2h\,\cos\omega t)\}.$$

Taking real parts of stress and strain,

$$\gamma = \gamma_o\ \cos\omega t$$
$$\tau = G\gamma_o\left(\cos\omega t - 2h\,\sin\omega t\right).$$

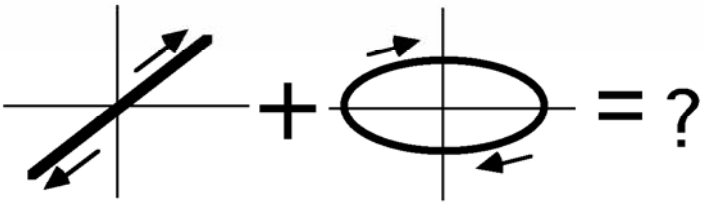

**Fig. 9.2** Elastic and plastic components in complex stress–strain model

The first term of stress is in phase with strain and stands for an elastic component. The second one is 90° earlier than strain, revealing the plastic component. See Fig. 9.2. According to Fig. 9.3,

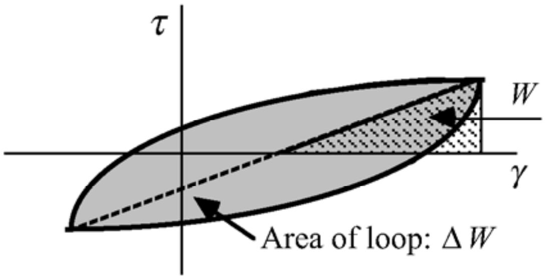

**Fig. 9.3** Soil-dynamic definition of damping ratio

$$\Delta W = \oint \tau\,\mathrm{d}r = \oint \tau \frac{\mathrm{d}r}{\mathrm{d}t}\ \mathrm{d}t$$
$$= -\omega G\gamma_o{}^2 \int_0^{2\pi} (\cos\omega t - 2h\ \sin\omega t)\sin\omega t\ \mathrm{d}t = 2\pi h G\gamma_o{}^2$$
$$W = \frac{G}{2}\gamma_o{}^2.$$

Note that $\Delta W$ is independent of loading frequency, which is consistent with real soil behavior (Sect. 6.2). Accordingly,

$$\frac{\Delta W}{4\pi W} = \frac{2\pi h G\gamma_o^2}{2\pi G\gamma_o^2} = h!\,.$$

Thus, damping ratio is constant, equal to $h$, independent of frequency, $\omega/(2\pi)$.

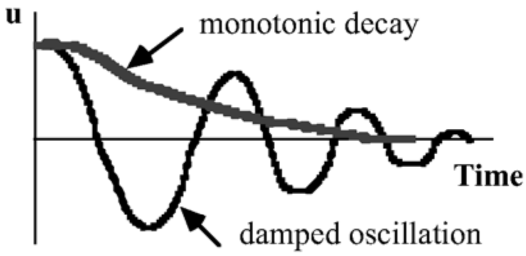

**Fig. 9.4** Two types of free movements

The damping ratio in soil dynamics is defined by using the area of a stress–strain loop. When the area of the loop is $\Delta W$, while the elastic energy is $W$ (Fig. 9.3), the damping ratio, $h$, is defined by

$$h = \frac{\Delta W}{4\pi W}.$$

This definition should not be confused with the structural-dynamic definition of "critical damping ratio."

Critical damping ratio: The equation of motion of a single-degree-of-freedom Voigt model

$$m\frac{\mathrm{d}^2u}{\mathrm{d}t^2}+c\frac{\mathrm{d}u}{\mathrm{d}t}+ku=0,$$

reveals that the nature of free vibration varies with the magnitude of $c$; damped oscillation when the critical damping ratio $c/(2\sqrt{mk})<1$ and monotonic decay when $c/(2\sqrt{mk})\geq 1$. See Fig. 9.4. Thus, the critical damping ratio should not be confused with damping ratio, $h$, in soil dynamics.

## 9.2 Damping Ratio in Soil Dynamics and Critical Damping Ratio

This section compares the damping ratio in soil dynamics and the critical damping ratio in structural dynamics. They are equal to each other when a Voigt model in structural dynamics (Fig. 9.5) is excited at a special frequency, as shown in what follows.

The area of hysteresis loop developed by a Voigt model increases in proportion to the frequency. It is interesting, however, that $\Delta W/(4\pi W)$ of a Voigt model is equal to the critical damping ratio, when it is subjected to a forced vibration under a certain circular frequency of $\omega$. The equation of motion is

$$m\frac{\mathrm{d}^2u}{\mathrm{d}t^2}+c\frac{\mathrm{d}u}{\mathrm{d}t}+ku=F\ \exp(\mathrm{i}\omega t),$$

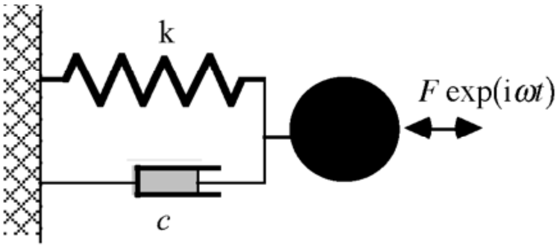

**Fig. 9.5** Voigt model undergoing forced excitation

where $F$ is a real number. By safely employing a harmonic solution for "$u$",

$$u=U\ \exp(\mathrm{i}\omega t)=U(\cos\omega t+\mathrm{i}\ \sin\omega t),$$

where $U$ is a real number. Hence,

$$\text{Force[in the Voigt Model]}=c\frac{\mathrm{d}u}{\mathrm{d}t}+ku=U(\mathrm{i}c\omega+k)\exp(\mathrm{i}\omega t).$$

Taking the real parts,

$$\mathrm{Re}(u)=U\cos\omega t\ \text{ and }\ \mathrm{Re(Force)}=U(k\cos\omega t-c\omega\sin\omega t).$$

The elastic energy and the energy loss per cycle are obtained as (Fig. 9.6)

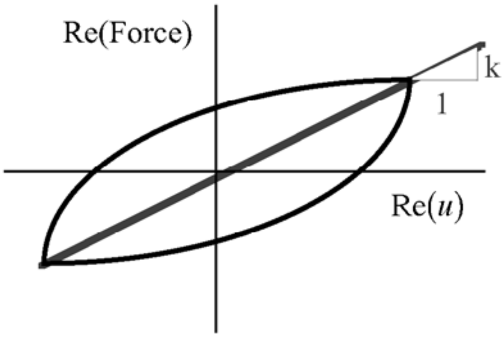

**Fig. 9.6** Force vs. displacement relationship

$$W=\frac{k}{2}U^2$$

$$\Delta W=\oint\mathrm{Re(Force)}d\{\mathrm{Re}(u)\}=U\int_0^{2\pi/\omega}(k\ \cos\omega t-c\omega\ \sin\omega t)\frac{\mathrm{d}\{\mathrm{Re}(u)\}}{\mathrm{d}t}\mathrm{d}t$$

$$=-U^2\omega\int_0^{2\pi/\omega}\left\{\frac{k}{2}\sin2\omega t-\frac{c\omega}{2}(1-\cos2\omega t)\right\}\mathrm{d}t=\pi c\omega U^2.$$

Thus, the energy loss per cycle in a Voigt model depends on the loading frequency. Consequently,

$$\frac{\Delta W}{4\pi W}=\frac{c\omega}{2k}. \qquad (9.1)$$

When the loading frequency is identical with the natural frequency,

$$\omega=\omega_0=\sqrt{k/m}\quad\text{and}\quad\frac{\Delta W}{4\pi W}=\frac{c}{2\sqrt{mk}},$$

which is identical with the structural-mechanic definition of critical damping ratio (Sect. 9.1).

## 9.3 Damped Oscillation of Complex-Modulus Model

The idea of complex modulus is used in a single-degree-of-freedom model (Fig. 9.7). The equation of motion in the course of free vibration is

$$m\frac{\mathrm{d}^2u}{\mathrm{d}t^2}+k(1+2\mathrm{i}h)u=0.$$

To derive its solution, $u=U\exp(\lambda t)$ is assumed. Then,

$$m\lambda^2+k(1+2\mathrm{i}h)=0$$

$$\lambda^2=-\frac{k}{m}(1+2\mathrm{i}h)=-\frac{k}{m}\sqrt{1+4h^2}\,\exp(\mathrm{i}\delta),$$

in which $\tan\delta\equiv 2h$. Therefore,

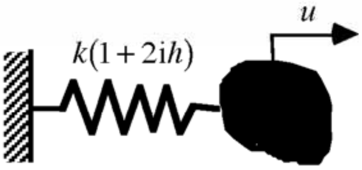

**Fig. 9.7** Free vibration of complex-modulus model

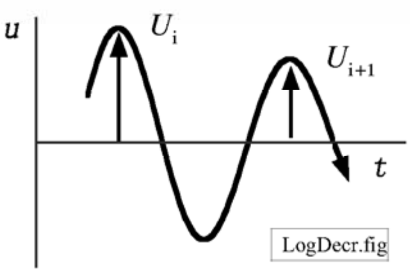

**Fig. 9.8** Definition of logarithmic decrement in free vibration

$$\lambda=\pm i\sqrt{\frac{k}{m}\sqrt{1+4h^2}}\left(\cos\frac{\delta}{2}+\mathrm{i}\,\sin\frac{\delta}{2}\right)=\pm\sqrt{\frac{k}{m}\sqrt{1+4h^2}}\left(\text{-}\sin\frac{\delta}{2}+\mathrm{i}\,\cos\frac{\delta}{2}\right).$$

Since a positive value in the real part of the solution of $\lambda$ gives an infinitely large displacement at an infinite time, only the negative solution is used. Therefore,

$$u=U\exp\left(\text{-}\sqrt{\frac{k}{m}\sqrt{1+4h^2}}\,\sin\frac{\delta}{2}\times t\right)\exp\left(\mathrm{i}\sqrt{\frac{k}{m}\sqrt{1+4h^2}}\,\cos\frac{\delta}{2}\times t\right).$$

Thus, a damped oscillation occurs, whatever the damping ratio ($h$) may be; the critical damping ratio < 1. The decay of amplitude during one period of free vibration

$$\text{Period}=\frac{2\pi}{\sqrt{\frac{k\sqrt{1+4h^2}}{m}}\cos\frac{\delta}{2}}$$

is derived as (see Fig. 9.8)

$$\frac{U_i}{U_{i+1}}=\exp\left(2\pi\tan\frac{\delta}{2}\right).$$

The logarithmic decrement is defined by $\log_e(U_i/U_{i+1})$

$$\log_e\frac{U_i}{U_{i+1}}=2\pi\,\tan\frac{\delta}{2}\approx\pi\,\tan\delta=2\pi h.$$

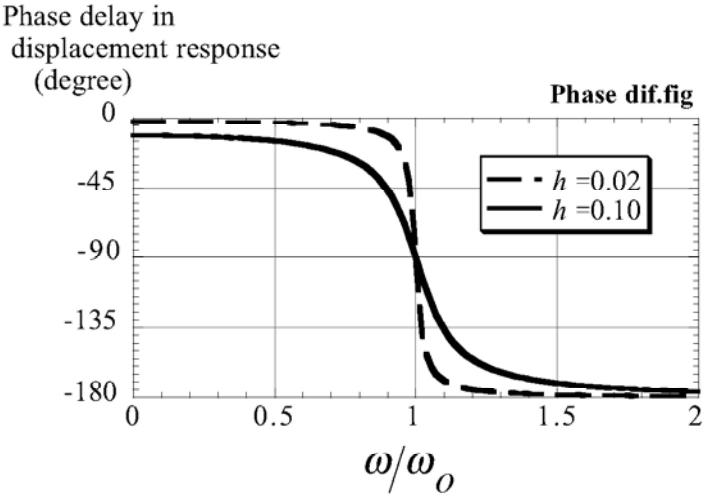

**Fig. 9.9** Phase delay of displacement in complex-modulus model

The logarithmic decrement is approximately proportional to "$h$" when damping is reasonably small. Upon forced vibration, in contrast,

$$m\frac{\mathrm{d}^2u}{\mathrm{d}t^2}+c\frac{\mathrm{d}u}{\mathrm{d}t}+ku=F_o\,\exp(\mathrm{i}\omega t)$$

The solution is derived by assuming $u=U\exp(\mathrm{i}\omega t)$,

$$u = \frac{F_o}{\left(k - m\omega^2\right)^2 + (2kh)^2}\left(k - m\omega^2 - 2kh\mathrm{i}\right)\exp(\mathrm{i}\omega t),$$

This means that the phase angle of displacement is behind the phase of force $(\omega t)$ due to "$-2kh\mathrm{i}$". The delay angle is given by

$$-\arctan\frac{2kh}{k - m\omega^2} = -\arctan\frac{2h}{1 - \left(\omega/\omega_o\right)^2},$$

which is illustrated in Fig. 9.9. At resonance, the delay is 90°.

## 9.4 Forced Oscillation of Complex-Modulus Model

Knowledge about dynamic response is useful in experimentally identifying material parameters. When a complex modulus model in Fig. 9.7 is subjected to a harmonic force, the equation of motion is given by

$$m\frac{\mathrm{d}^2u}{\mathrm{d}t^2}+k(1+2ih)u=F\exp(\mathrm{i}\omega t)$$

where $F > 0$ is a real number. The solution is derived as

$$u=\frac{F}{\left(k-m\omega^2\right)+2kh\mathrm{i}}\exp(\mathrm{i}\omega t)$$

and the amplitude of displacement is found to be

$$U=|u|=\frac{F}{\sqrt{\left(k-m\omega^2\right)^2+4k^2h^2}}=\frac{1}{2h}\times\frac{F}{k}\times\frac{1}{\sqrt{1+\left(\frac{1-\omega^2/\omega_o{}^2}{2h}\right)^2}},$$

where $F/k$ is the displacement under a static force. This equation shows that

1. The resonance occurs at $\omega=\omega_o=\sqrt{k/m}$ for which the amplitude of motion is $(1/2h)$ times the static displacement ($F/k$). Thus, the value of "$h$" is experimentally determined by comparing the resonant amplitude with the static displacement. When the static displacement cannot be measured, use the second method as below.
2. The circular frequencies at which the amplitude of motion is $1/\sqrt{2}$ times the resonance amplitude are denoted by $\omega_-$ and $\omega_+$

$$\begin{Bmatrix}\omega_+\\ \omega_-\end{Bmatrix}=\omega_0\sqrt{1\pm 2h}\,.$$

By detecting experimentally these two special frequencies, the damping ratio of any structure can be determined

$$h=\left\{\left(\frac{\omega_+}{\omega_0}\right)^2-\left(\frac{\omega_-}{\omega_0}\right)^2\right\}\bigg/4.$$

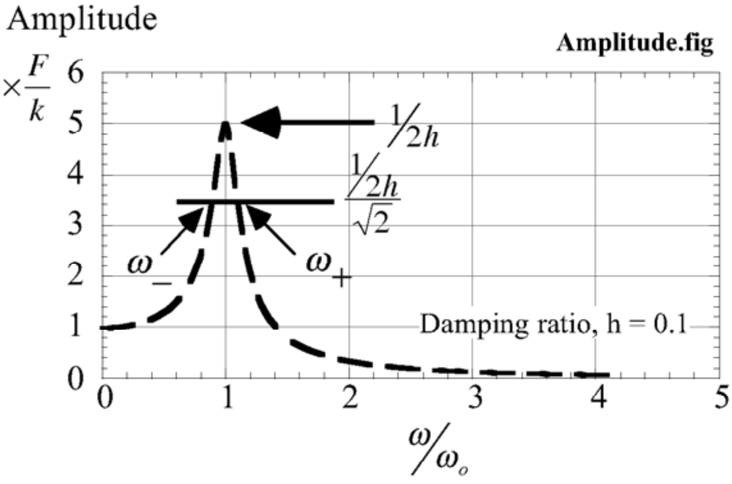

**Fig. 9.10** Amplitude of complex-modulus model

See Fig. 9.10. The idea described in this page is used in the interpretation of resonant column tests of soils in which unknown soil parameters of shear modulus and damping ratio are determined.

The complex-modulus model concerns only dynamic phenomena. For example, substitute $\omega = 0$ into the above equations to see the amplitude of motion not being equal to the static displacement of $F/k$.

# Exercise 3 Calculation of Amplification Factor

See a three-layered ground in the figure.

1. Calculate the amplification of Amp(2*E*) and Amp(*E*+*F*).
2. What is the ground motion at the rock outcrop (露頭)?

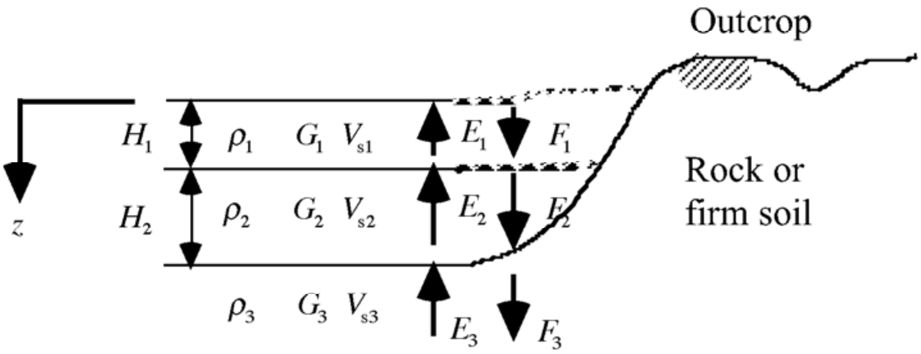

Answer! →

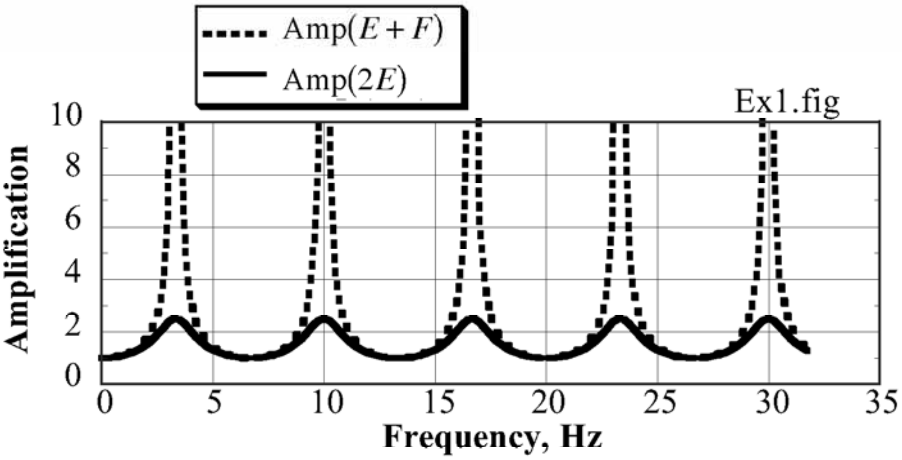

## 9.5 Wave Propagation in Complex-Modulus Medium

The equation of wave propagation is going to be solved here for a case of complex-modulus material. When the modulus is given by $G(1+2\mathrm{i}h)$, which is uniform in a ground,

$$\frac{\partial^2 u}{\partial t^2} = V_\mathrm{s}^2 (1+2\mathrm{i}h) \frac{\partial^2 u}{\partial z^2}$$

where $V_\mathrm{s} = \sqrt{G/\rho}$ and $\delta = \arctan(2h)$. Hence,

$$\frac{\partial^2 u}{\partial t^2} = V_\mathrm{s}^2 \left(1+4h^2\right)^{1/2} \exp(\mathrm{i}\delta) \frac{\partial^2 u}{\partial z^2}.$$

The harmonic solution for this is symbolically described as

$$u = E \exp\left\{ \mathrm{i}\omega \left( t + \frac{z}{V_\mathrm{s}^*} \right) \right\} + F \exp\left\{ \mathrm{i}\omega \left( t - \frac{z}{V_\mathrm{s}^*} \right) \right\}, \tag{9.2}$$

in which $V_\mathrm{s}^* = V_\mathrm{s}\left(1+4h^2\right)^{1/4} \exp(\mathrm{i}\delta/2)$ and $\exp(\mathrm{i}\delta/2) = \cos\frac{\delta}{2} + i \sin\frac{\delta}{2}$. The "*E*" and "*F*" terms stand for the upward and downward wave propagations, respectively. Then, more in detail, the "*E*" term is described as

$$u = E \exp\left[ i\omega \left\{ t + \frac{\left( \cos\frac{\delta}{2} - i \sin\frac{\delta}{2} \right) z}{V_\mathrm{s}\left(1+4h^2\right)^{1/4}} \right\} \right] = E \exp\left\{ \frac{\omega \left( \sin\frac{\delta}{2} \right) z}{V_\mathrm{s}\left(1+4h^2\right)^{1/4}} \right\} \exp\left[ i\omega \left\{ t + \frac{\left( \cos\frac{\delta}{2} \right) z}{V_\mathrm{s}\left(1+4h^2\right)^{1/4}} \right\} \right]. \tag{9.3}$$

The associating shear stress of "E" component is given by

$$\begin{aligned} \tau &= G(1+2\mathrm{i}h) \frac{\partial u}{\partial z} \\ &= E \frac{\mathrm{i}\omega\rho V_\mathrm{s}\left(1+4h^2\right)^{1/2} \exp(\mathrm{i}\delta) \left( \cos\frac{\delta}{2} - \mathrm{i} \sin\frac{\delta}{2} \right)}{\left(1+4h^2\right)^{1/4}} \exp\left\{ \frac{\left( \omega \sin\frac{\delta}{2} \right) z}{V_\mathrm{s}\left(1+4h^2\right)^{1/4}} \right\} \exp\left[ \mathrm{i}\omega \left\{ t + \frac{\left( \cos\frac{\delta}{2} \right) z}{V_\mathrm{s}\left(1+4h^2\right)^{1/4}} \right\} \right] \\ &= E \times \mathrm{i}\omega\rho V_\mathrm{s}\left(1+4h^2\right)^{1/4} \exp\left( \mathrm{i}\frac{\delta}{2} \right) \exp\left\{ \frac{\left( \omega \sin\frac{\delta}{2} \right) z}{V_\mathrm{s}\left(1+4h^2\right)^{1/4}} \right\} \exp\left[ \mathrm{i}\omega \left\{ t + \frac{\left( \cos\frac{\delta}{2} \right) z}{V_\mathrm{s}\left(1+4h^2\right)^{1/4}} \right\} \right]. \end{aligned} \tag{9.4}$$

The wave length, $L$, is determined by

$$\omega \frac{\left( \cos\frac{\delta}{2} \right) L}{V_\mathrm{s}\left(1+4h^2\right)^{1/4}} = 2\pi \quad \text{and} \quad L = \frac{2\pi V_\mathrm{s}\left(1+4h^2\right)^{1/4}}{\omega \cos\frac{\delta}{2}}. \tag{9.5}$$

For the "F" term of shear stress, "*z*" above is replaced by "–*z*" By using the boundary condition of zero shear stress at the surface ($z = 0$),

$\tau(z=0) = (E-F)\times \mathrm{i}\omega\rho V_{\mathrm{s}}\left(1+4h^2\right)^{1/4} \exp(\mathrm{i}\delta/2)$ and, consequently, $E=F$.

Thus, the solution of wave propagation equation is obtained

$$u = E\left[\underline{\exp\left\{\frac{\omega\left(\sin\frac{\delta}{2}\right)z}{V_{\mathrm{s}}\left(1+4h^2\right)^{1/4}}\right\}}\exp\left[\mathrm{i}\omega\left\{t+\frac{\left(\cos\frac{\delta}{2}\right)z}{V_{\mathrm{s}}\left(1+4h^2\right)^{1/4}}\right\}\right] + \underline{\exp\left\{\frac{-\omega\left(\sin\frac{\delta}{2}\right)z}{V_{\mathrm{s}}\left(1+4h^2\right)^{1/4}}\right\}}\exp\left[\mathrm{i}\omega\left\{t-\frac{\left(\cos\frac{\delta}{2}\right)z}{V_{\mathrm{s}}\left(1+4h^2\right)^{1/4}}\right\}\right]\right].$$

Both components on the right-hand side have exponential multipliers (indicated by dashed underlines). They stand for the decay of wave with a propagation distance. It means that he amplitude is reduced at a rate of $\exp\left\{-2\pi\ \tan\left(\delta/2\right)\right\}$ per one wave length, $L$.

The velocity of wave propagation is consequently derived

$$\text{Velocity } = \frac{\text{Wave length } L}{\text{Period } (=2\pi/\omega)} = V_{\mathrm{s}}\frac{\left(1+4h^2\right)^{1/4}}{\cos\frac{\delta}{2}} = V_{\mathrm{s}}\frac{\left(1+\tan^2\delta\right)^{1/4}}{\cos\frac{\delta}{2}} = \frac{V_{\mathrm{s}}}{\sqrt{\cos\delta}\ \cos\frac{\delta}{2}}\ . \tag{9.6}$$

## 9.6 Solution of Real Numbers in Complex-Modulus Ground

The solution in Sect. 9.5 is further studied. Figure 9.11 illustrates the concept of a two-layered soil deposit. The surface soil is soft, while the bottom one is a rigid material such as base rock, tertiary deposit, or pleistocene material.

$$u = 2E_1\left[\cosh\left\{\frac{\omega \sin\frac{\delta}{2}\times z}{V_s\left(1+4h^2\right)^{1/4}}\right\}\cos\left\{\frac{\omega \cos\frac{\delta}{2}\times z}{V_s\left(1+4h^2\right)^{1/4}}\right\} + i\,\sinh\left\{\frac{\omega \sin\frac{\delta}{2}\times z}{V_s\left(1+4h^2\right)^{1/4}}\right\}\sin\left\{\frac{\omega \cos\frac{\delta}{2}\times z}{V_s\left(1+4h^2\right)^{1/4}}\right\}\right]\exp(i\omega t)$$

$$\tau = 2E_1\rho V_s\left(1+4h^2\right)^{1/4}\ \exp\frac{i\delta}{2}$$
$$\times\left[\sinh\left\{\frac{\omega \sin\frac{\delta}{2}\times z}{V_s\left(1+4h^2\right)^{1/4}}\right\}\cos\left\{\frac{\omega \cos\frac{\delta}{2}\times z}{V_s\left(1+4h^2\right)^{1/4}}\right\} + i\,\cosh\left\{\frac{\omega \sin\frac{\delta}{2}\times z}{V_s\left(1+4h^2\right)^{1/4}}\right\}\sin\left\{\frac{\omega \cos\frac{\delta}{2}\times z}{V_s\left(1+4h^2\right)^{1/4}}\right\}\right]\exp(i\omega t)\ .$$

The amplification of Amp($E$+$F$) is given by the ratio

$$\mathrm{Amp}(E+F) \equiv \frac{\left|u(z=0)\right|}{\left|u(z=H)\right|}$$

and is illustrated in Fig. 9.12. Note that the amplification is smaller at higher frequency. This is because the wave length is shorter, the number of cycles during wave propagation is greater, and, in accordance with the number of cycles in the course of wave propagation, the amount of energy loss is increased. This disappearance of high-frequency components is in good contrast with the elastic solution in Sect. 6.8.

For plotting time histories of displacement or stress, the real parts of the above equations are employed.

Note that Amp($E$+$F$) simply indicates the dynamic behavior of the surface deposit; it does not account for the local geology in which there is a harder base layer underneath. Use Amp(2$E$) in Sect. 9.7 when effects of such a local geological structure has to be investigated.

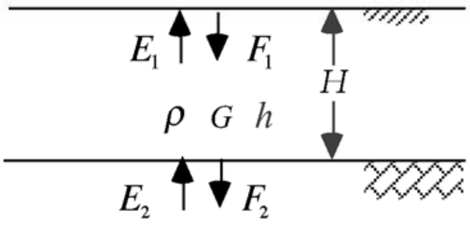

**Fig. 9.11** Model of level ground with complex modulus

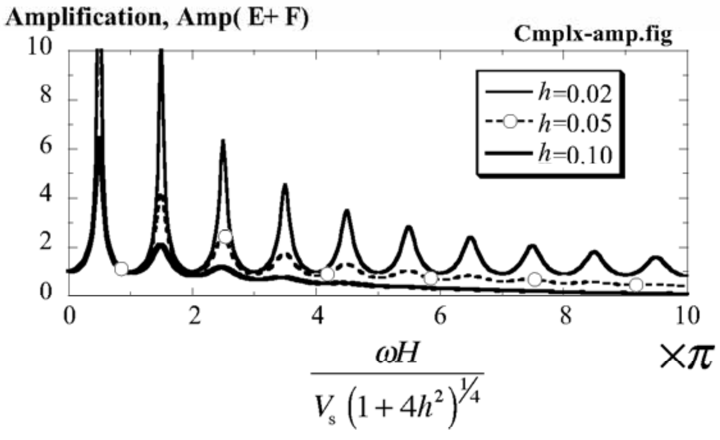

**Fig. 9.12** Amplification in complex-modulus ground

## 9.7 Outcrop Amplification in Complex-Modulus Ground

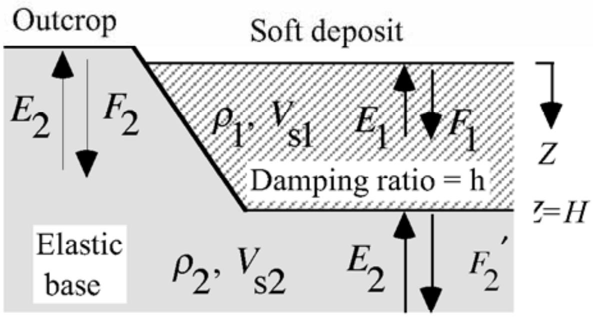

**Fig. 9.13** Two-layered alluvium

Study is made of the propagation of SH wave (Sect. 4.2) in a two-layered complex-modulus subsoil; see Fig. 9.13 for notation. The amplitudes of motion at the outcrop and at the surface of soft alluvium are compared. When a harmonic motion is considered, the motion in the alluvium is given by

$$u_1 = E_1\left[\exp\left\{\mathrm{i}\omega\left(t+\frac{z}{V_{s1}^*}\right)\right\}+\exp\left\{\mathrm{i}\omega\left(t-\frac{z}{V_{s1}^*}\right)\right\}\right], \tag{9.7}$$

where $V_{si}^* = V_{s1}\left(1+4h^2\right)^{1/4}\exp(\mathrm{i}\delta/2)$ and $\delta = \arctan(2h)$, Sect. 9.5. See that the amplitude of $u$ is $2E_1$ at the surface ($z = 0$). Furthermore, the shear stress is given by

$$\tau_1 = G_1(1+2ih)\frac{\partial u_1}{\partial z} = G_1(1+2ih)\frac{i\omega}{Vs_1^*}E_1\left[\exp\left\{i\omega\left(t+\frac{z}{Vs_1^*}\right)\right\}-\exp\left\{i\omega\left(t-\frac{z}{Vs_1^*}\right)\right\}\right], \tag{9.8}$$

in which the boundary condition at the surface (*shear stress = 0*) is accounted for. Similarly, the solution in the elastic base beneath the alluvium is given by

*Amp(2E) is a more direct index than Amp(E+F) of the effects of local geology.*

$$u_2 = E_2\,\exp\left\{\mathrm{i}\omega\left(t+\frac{z-H}{V_{s2}}\right)\right\}+F_2'\,\exp\left\{\mathrm{i}\omega\left(t-\frac{z-H}{V_{s2}}\right)\right\} \tag{9.9}$$

$$\tau_2 = G_2\frac{\mathrm{i}\omega}{V_{s2}}\left[E_2\,\exp\left\{\mathrm{i}\omega\left(t+\frac{z-H}{V_{s2}}\right)\right\}-F_2'\,\exp\left\{\mathrm{i}\omega\left(t-\frac{z-H}{V_{s2}}\right)\right\}\right]. \tag{9.10}$$

Since both displacement and shear stress are continuous at $z = H$, ( (9.7) = (9.9) and (9.8) = (9.10), $E_2$ and $F_2$' are solved in terms of $E_1$. Consequently,

$$\left\{\frac{1}{\mathrm{Amp}(2E)}\right\}^2 = \left|\frac{2E_2}{2E_1}\right|^2 = \frac{1}{2}\left\{\cosh\left(2x\,\sin\frac{\delta}{2}\right)+\cos\left(2x\,\cos\frac{\delta}{2}\right)\right\}+\frac{\rho_1 V_{s1}}{\rho_2 V_{s2}}\left(1+4h^2\right)^{1/4}\left\{\cos\frac{\delta}{2}\sinh\left(2x\,\sin\frac{\delta}{2}\right)\right.$$

$$\left.-\sin\frac{\delta}{2}\sin\left(2x\,\cos\frac{\delta}{2}\right)\right\}+\frac{1}{2}\left(\frac{\rho_1 V_{s1}}{\rho_2 V_{s2}}\right)^2\left(1+4h^2\right)^{1/2}\left\{\cosh\left(2x\,\sin\frac{\delta}{2}\right)-\cos\left(2x\,\cos\frac{\delta}{2}\right)\right\}, \tag{9.11}$$

where $x = (\omega H)\Big/\left\{V_{s1}\left(1+4h^2\right)^{1/4}\right\}$. The outcrop amplification is obtained by Amp(2$E$)= $\left|2E_1/2E_2\right|$, which is demonstrated in Fig. 9.14 for two values of the impedance ratio, $\rho_1 V_{s1}/\rho_2 V_{s2}$. The amplification is greater when the alluvium is softer (impedance ratio = 0.1) and the damping ratio is smaller.

It is interesting that very soft ground with a small value of $V_s$ has a large value of $\omega H/V_s$ and consequently low amplification. When the intensity of shaking is very strong, moreover, the induced shear strain is large and consequently the damping ratio, $h$, becomes substantial (nonlinearity in Sect. 10.8 and Sect. 10.15). This situation leads to the amplification, that may be less than 1.0. Idriss (1990) combined dynamic analyses and measured earthquake records to suggest that this idea may be the reality (Fig. 9.15).

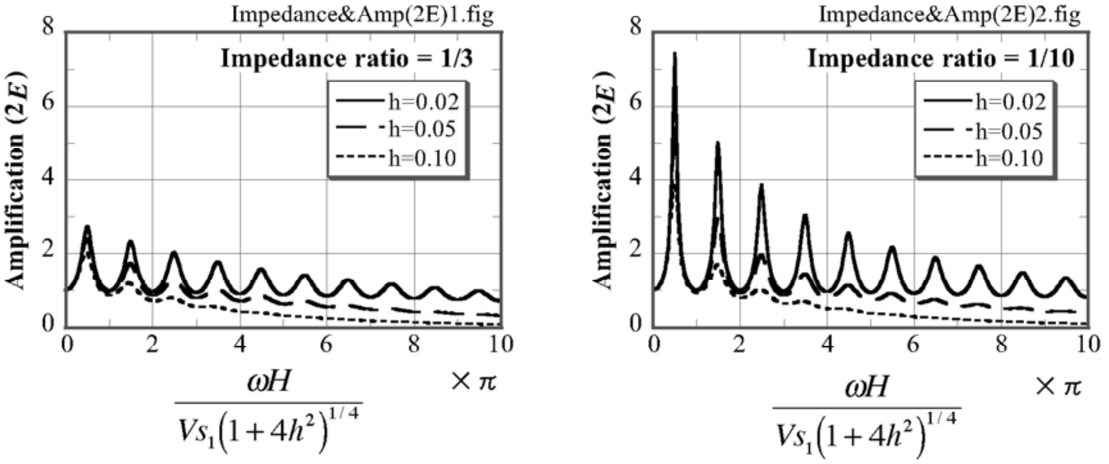

**Fig. 9.14** Effects of impedance ratio on amplification in surface deposit

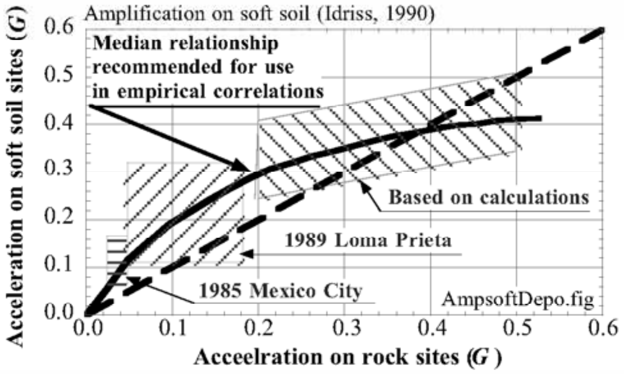

**Fig. 9.15** Amplification of soft ground changing with intensity of outcrop excitation (drawn after Idriss, 1990)

## 9.8 Exercise No. 4 Response Analysis on Multilayered Deposits

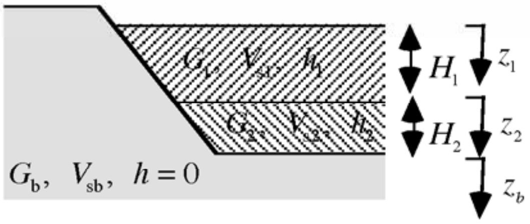

First develop a computer program that can solve a linear equation

$$\begin{bmatrix} C_{11} & C_{12} \\ C_{21} & C_{22} \end{bmatrix} \begin{Bmatrix} x_1 \\ x_2 \end{Bmatrix} = \begin{Bmatrix} q_1 \\ q_2 \end{Bmatrix},$$

in which all numbers are complex 複素数. Use the conventional Gaussian elimination ガウスの消去法 and do not be afraid of a singular matrix, $C_{11}C_{22} - C_{12}C_{21} = 0$.

Assume then a stratification of soil with two alluvial layers resting on an engineering base rock (see the illustration above). The nonlinear stress–strain relationship of soils is expressed by a complex-modulus model $G^*=G(1+2ih)$. The base is made of an elastic medium.

1. Calculate the amplification Amp($2E$) of the surface motion against the outcrop motion by taking into account the continuity of displacement and shear stress at the interfaces. For convenience of calculation use vertical coordinates of $z_1$, $z_2$, and $z_b$ in respective layers.
2. Plot Amp($2E$) then over a range of normalized frequency of $\omega H_1/V_{s1}$=0–10, for a special case of
    - – constant $\rho$ of soils from the surface to the base
    - – $V_{s1}/V_{s2} = 1/3$ and $V_{s2}/V_{sb} = 1/3$
    - – Damping ratio : $h_1 = 0.10$ and $h_2 = 0.03$
    - – $H_1 = H_2$.

It is recommended to run all the calculations by using complex numbers. Keep the computer program for this assignment, and if you make any, for a later assignment.

## 9.9 Variation of Shear Modulus at Interface of Soil Layers

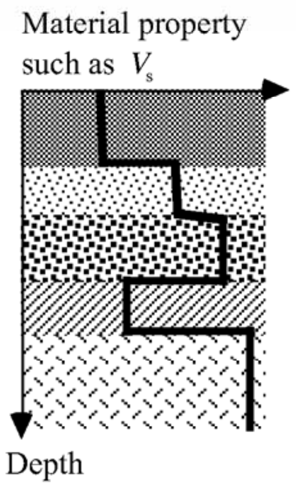

**Fig. 9.16** Modelling of subsoil by uniform layers

It is a common practice in current dynamic analyses to divide subsoil into homogeneous layers (or finite elements). Consequently, material properties are discontinuous at layer interfaces, see Fig. 9.16. Section 4.10 indicated that discontinuity in material properties generates wave reflection.

Material properties of artificially reclaimed soil and natural alluvial deposits were studied in Tokyo Bay area by the Association for Development of Earthquake Prediction, Tokyo. Undisturbed soil samples were collected to measure shear modulus, $G_{max}$, as well as gradation (粒度分布) and they were compared with $V_s$ which was measured insitu by a suspension technique (Sect. 8.2).

Upon artificial reclamation, the reclaimed soil and the existing seabed soil are different. This point is evidenced by the drastic variation of fines content at around 9 m depth (Fig. 9.17). The in-situ measured $V_s$ is continuous, in contrast, at this depth (Fig. 9.18) probably because the effective stress is continuous in the vertical direction. Hence, the discontinuous modeling as illustrated in Fig. 9.16 at the interface may not be very realistic and reflects earthquake energy back into the lower strata, reducing shaking energy in the surface soil.

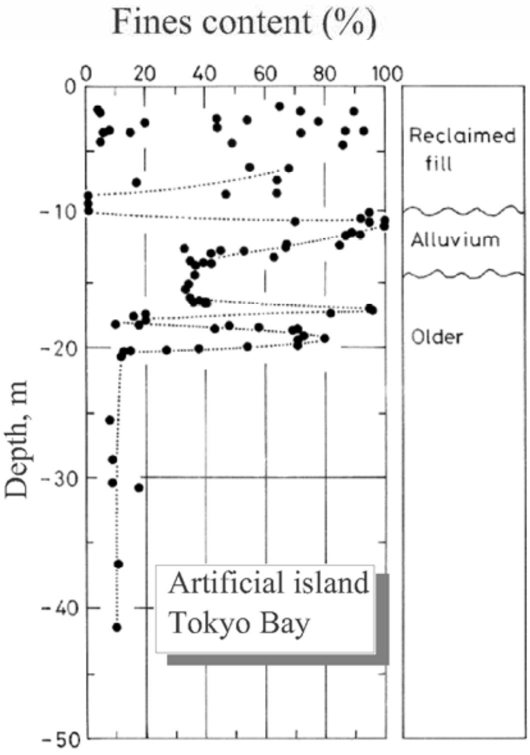

**Fig. 9.17** Change of fines content at interface of natural deposit and artificial fill

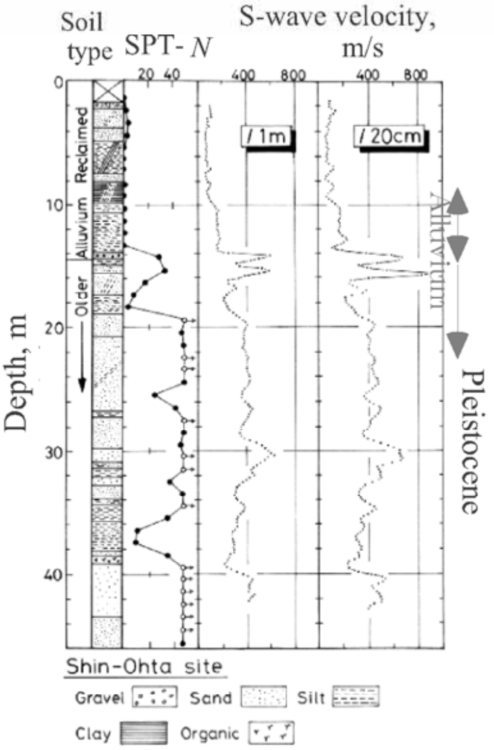

**Fig. 9.18** Discontinuity of shear wave velocity at interface of natural deposit and artificial fill

The alluvial layer exhibits continuous variation in both fines content and S wave velocity. This seems consistent with the continuity of age of soil as well as the continuity of effective stress. Thus, the discontinuous modelling in Fig. 9.16 is not realistic.

The interface between the alluvium and the pleistocene deposit (15 m below surface) demonstrates a remarkable change in fines content due to discontinuity in age and material type (unconformity 不整合);

older deposit was eroded while the sea level was low and then new material started to deposit. The associating variation of S wave velocity ($V_s$) is so significant as well, and may be modeled by a discontinuity (Fig. 9.11) for practice.

The underlying pleistocene deposits has some significant change in fines content due probably to the variation of sedimentary environment. However, $V_s$ is still continuous, although it varies with depth.

From these observations, it seems reasonable to state that the real natural ground has a continuous variation of S wave velocity and, in general, the discontinuous modelling may not be appropriate. Discontinuous modelling seems reasonable only at unconformity where both age and type of soil vary suddenly. The effects of continuous and discontinuous modellings were studied in dynamic analyses by the author (Towhata, 1996).

## 9.10 Equivalent Linear Modeling

The major nonlinearity in stress–strain behavior of soil is detected in two points

1. Shear modulus, $G$ (more precisely, secant shear modulus) that decreases as the strain amplitude increases.
2. A hysteresis loop in shear stress–strain relationship and the damping ratio that increases with the strain amplitude.

The nonlinearity is taken into account in analysis in several ways. First, the stress–strain behavior can be modeled in detail by elastoplasticity (Chap. 10) possibly combined with viscosity. This approach requires many input parameters, which are determined by elaborate laboratory soil testing on specimens of good quality. Therefore, there is a general impression that this approach is good but time consuming. Moreover, it is common that many elastoplastic models give different results.

The second method is the equivalent linear method for which a closed-form solution of motion is available (Sect. 9.5). Although there are many limitations, this approach has been widely used because of its easy use. Therefore, two types of soil data have to be prepared:

1. Shear modulus at small strain amplitude that is typically $10^{-6}$ (=$10^{-4}$%) or less. Most field investigation technologies (downhole survey, PS logging, etc. in Chap. 7) generate this magnitude of strain. Hence, $V_s$ measured insitu directly gives this small-strain modulus. This modulus is denoted by $G_{max}$ or $G_0 = \rho V_s^2$.
2. Nonlinearity of soil expressed by variation of $G$ and $h$ (damping ratio) with the strain amplitude $\gamma_a$ during cyclic loading. Since $G_{max}$ is already known above, test data on variation of $G/G_{max}$ and $h$ against $\log_{10}(\gamma_a)$ is widely used. See Fig. 9.19.

Although the real soil behavior under cyclic loading is much more complicated than expressed by $G$ and $h$, the dynamic response of ground is most strongly affected by these two parameters.

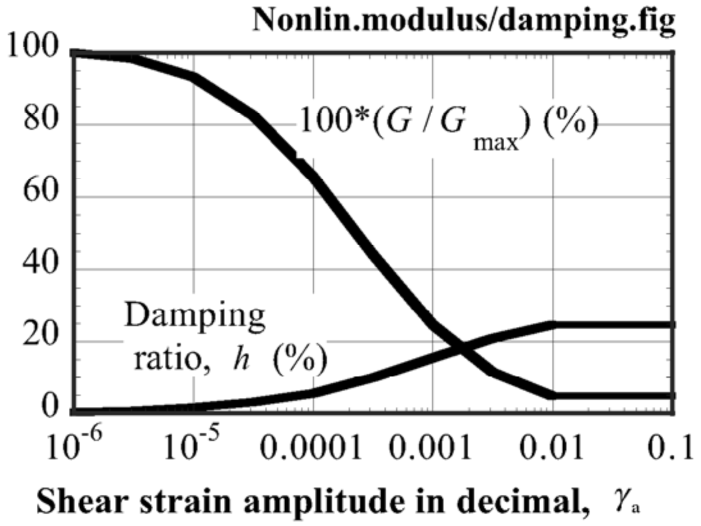

**Fig. 9.19** Example of soil data on nonlinear stress-strain behaviour (0.01 strain = 1% strain)

Many laboratory tests have been carried out to measure the data in such a manner as shown in Fig. 9.19. In this sense, the equivalent linear modeling in terms of $\tau = G(1+2ih)\gamma$ is a standard approach to soil dynamics. It is fortunate that $G/G_{max}$ and $h$ vs. strain curves are not much affected by most soil conditions, e.g., effective stress level, fines content, overconsolidation, etc. The effects of these factors appear in $G_{max}$ itself. Therefore, only $G_{max}$ should be determined with reference to insitu investigation (原位置試験). Only soil types, sand or clay, affect the shape of curves (later topic).

In practice, the curves in Fig. 9.19 are seldom measured directly. They are obtained from literatures reported on soils that are similar to the concerned one.

## 9.11 Theory of Fourier Series

Although the time history of a real earthquake motion is irregular, the equivalent linear technique of dynamic response analysis makes use of a harmonic base motion (Sect. 9.1). This is because any irregular time history can be divided into harmonic components by using the theory of Fourier series. Response analysis is made of harmonic components and the calculated responses are added together to obtain an irregular response.

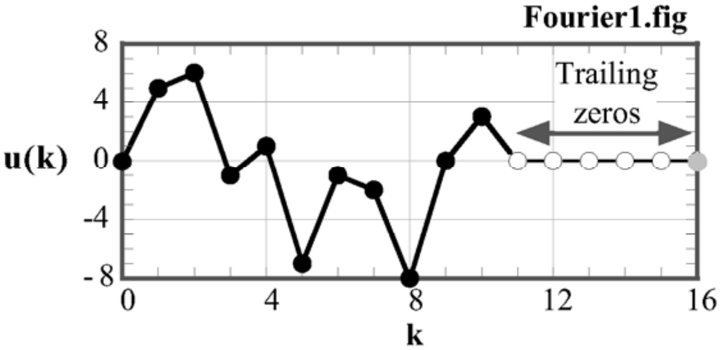

**Fig. 9.20** Example of time history of ground mothion, $u(k)$

Discussion is made of a Fourier series expansion of 16 data in Fig. 9.20; $u(k)$, k = 0–15. Note that an identical time history is repeated before k = 0 and after k = 16 due to the nature of harmonic functions (*sin* and *cos*). The Fourier series of this time history is given by summation of the following terms,

$i = \sqrt{-1}$

conjugate

| | Series |
|---|---|
| $u(k) = -0.25$ | 0 |
| $+(1.22+0.24i)\exp\left(\frac{2\pi i}{16}k\right)$ | 1 |
| $+(-0.08-1.20i)\exp\left(\frac{4\pi i}{16}k\right)$ | 2 |
| $+(0.14-0.39i)\exp\left(\frac{6\pi i}{16}k\right)$ | 3 |
| $+(-0.94-0.06i)\exp\left(\frac{8\pi i}{16}k\right)$ | 4 |
| $+(0.50-0.34i)\exp\left(\frac{10\pi i}{16}k\right)$ | 5 |
| $+(-1.05+0.05i)\exp\left(\frac{12\pi i}{16}k\right)$ | 6 |
| $+(0.13+0.54i)\exp\left(\frac{14\pi i}{16}k\right)$ | 7 |
| $+0.38\exp\left(\frac{16\pi i}{16}k\right)$ | Nyquist, 8 |
| $+(0.13-0.54i)\exp\left(\frac{-14\pi i}{16}k\right)$ | 9 |
| $+(-1.05-0.05i)\exp\left(\frac{-12\pi i}{16}k\right)$ | 10 |
| $+(0.50+0.34i)\exp\left(\frac{-10\pi i}{16}k\right)$ | 11 |
| $+(-0.94+0.06i)\exp\left(\frac{-8\pi i}{16}k\right)$ | 12 |
| $+(0.14+0.39i)\exp\left(\frac{-6\pi i}{16}k\right)$ | 13 |
| $+(-0.08+1.20i)\exp\left(\frac{-4\pi i}{16}k\right)$ | 14 |
| $+(1.22-0.24i)\exp\left(\frac{-2\pi i}{16}k\right)$ | 15 |

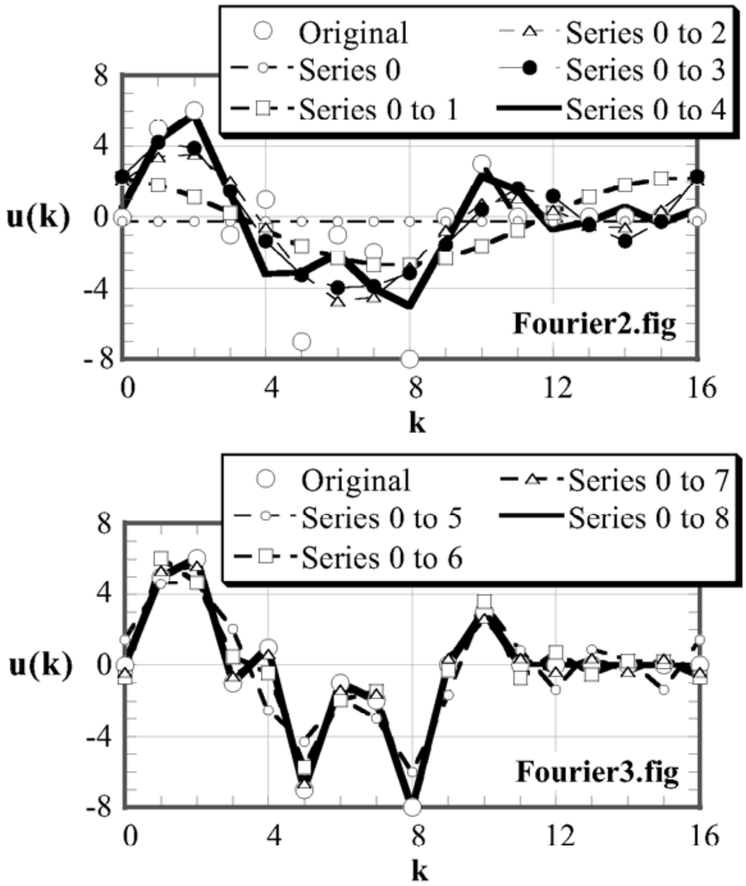

**Fig. 9.21** Convergence of Fourier series

See the conjugate (複素共役) relationships of complex coefficients. The middle of the above series (Series 8) has the highest frequency. The frequency of this component is called the Nyquist frequency. Figure 9.21 shows that the Fourier series expansion approaches the original function as components of higher frequencies are added. Trailing zeros in Fig. 9.20 is added to the original time history of earthquake motion in order (1) to account for the fact that the earthquake motion ceases after some time and (2) to make the total number of data a power of 2 (2のベキ) such as 256, 512, and 1,024 that make easy the fast Fourier transformation (FFT).

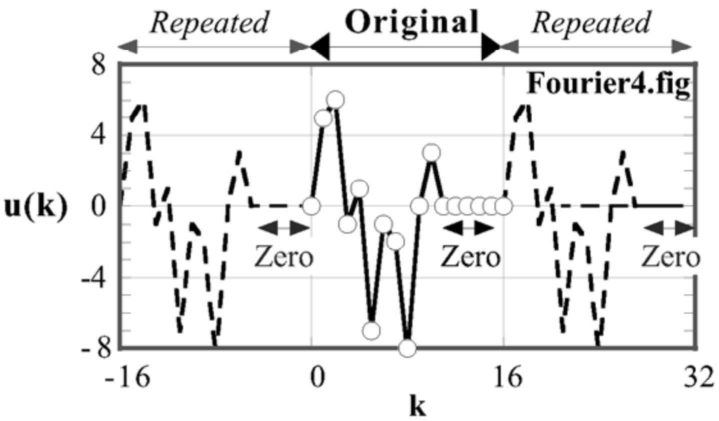

**Fig. 9.22** Repeated nature of Fourier series

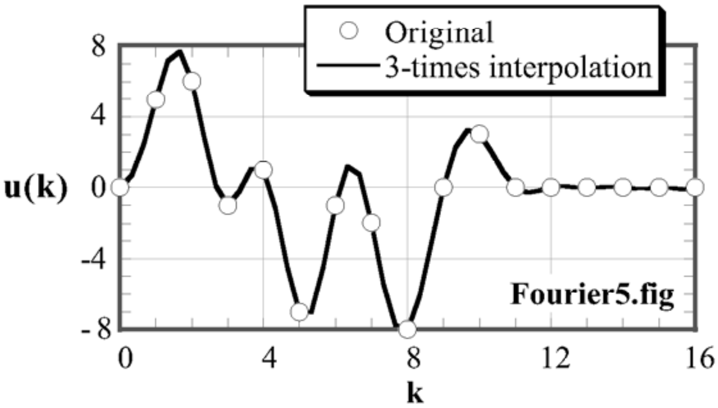

**Fig. 9.23** Interpolated time history of Fourier series

In principle, a Fourier series consists of *sin* and *cos* functions.

$$u(k) = \sum_{m=0}^{N-1} C_m \exp\left(\frac{2\pi mk}{N} i\right) = \sum_{m=0}^{N-1} C_m \left(\cos\frac{2\pi mk}{N} + i \sin\frac{2\pi mk}{N}\right), \quad (9.12)$$

where k = 0, 1, 2⋯N-1 and
$C_{N-m} = C_m^*$: conjugate relationship.

Note that each component with “k” in (9.12) has a period of

$$\frac{2\pi m \times \text{Period}}{N} = 2\pi$$

$$\text{Period} = \frac{N}{m}. \quad (9.13)$$

if m≤N/2.

Being a combination of periodical sin and cos functions, (9.12) means that exactly identical u(k)s appear after a certain number. Figure 9.22 illustrates this nature. Note that the trailing zeros effectively separate two neighboring time histories. Without zeros, the earthquake motion in the analysis is repeated without a stationary period and consequently the calculated response would be an overestimation. Those zeros erase the influence of the previous cycle of the imaginary earthquake (from $k = -16$ to $-1$ in Fig. 9.22).

Therefore, a sufficient number of trailing zeros should be added to the input motion data. Moreover, the technique of “fast Fourier transformation,” which accelerates the equivalent linear analysis, needs to make the total number of motion data equal to any power of 2, e.g., 512, 1,024, 2,048, etc. Since the number of given earthquake motion data is not necessarily a power of 2, the trailing zeros are used to satisfy the requirement from FFT.

In Fig. 9.23, the values of the Fourier series expansion were calculated at interpolated points of k = 1/3, 2/3, 4/3, 5/3, etc. By comparing the interpolated values with the original time history, it is found that the new magnitude of the interpolated motion is somewhat greater than the original one. Therefore, the use of the equivalent linear analysis with Fourier series expansion may overestimate the magnitude of input motion and, accordingly, the response of the surface subsoil during earthquakes.

## 9.12 Spectrum Analysis by Fourier Series

The theory of Fourier series has been applied to interpretation of earthquake motion records. Figure 9.24 shows the time history of acceleration at the top of an alluvial deposit (depth being GL –1m) in Tokyo during the 1987 Chiba-ken-Toho-oki (千葉県東方沖地震) earthquake. It may be seen that this motion has a predominant period of around 1.0 s. This surface motion is compared with the motion at the bottom of the alluvial layer (at the depth of GL –89 m) in Fig. 9.25. While the intensity of motion is much weaker in the bottom motion (Fig. 9.25), the predominant period of around 1.0 s is not evident. It seems that the motion of 1.0 s period was produced by the amplification in the alluvial soil (Sect. 6.8).

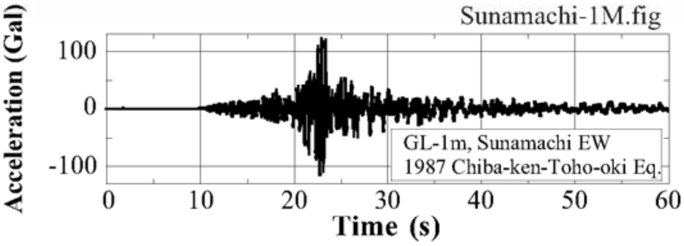

**Fig. 9.24** Time history of surface acceleration at Sunamachi site in Tokyo during the 1987 Chiba-ken-Toho-oki earthquake

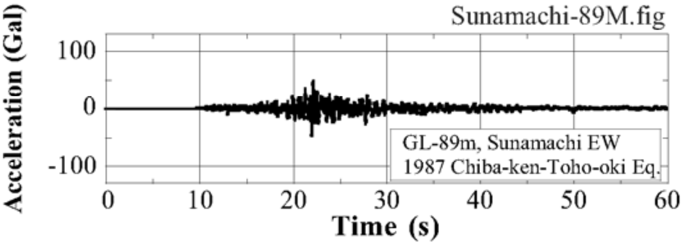

**Fig. 9.25** Time history of acceleration at the bottom of Sunamachi site in Tokyo during the 1987 Chiba-ken-Toho-oki earthquake

The time history of an earthquake motion record is expressed by means of Fourier series

$$u(t)=\sum_{m=0}^{N-1} C_m\left(\cos\frac{2\pi mt}{T}+i\ \sin\frac{2\pi mt}{T}\right) \quad \text{or} \quad u(k\Delta t)=\sum_{m=0}^{N-1} C_m\left(\cos\frac{2\pi mk\Delta t}{T}+i\ \sin\frac{2\pi mk\Delta t}{T}\right), \quad (9.14)$$

in which the time interval of the original digital data is $\Delta t$ and the total number of data is $N$; hence, the entire duration time of the record is $T = N\Delta t$. Therefore, each of the component with “m” has its own period of $T/m$ and the frequency of $m/T$ (Hz). On the other hand, the absolute value of $C_m$ in (9.14) stands for the intensity of each frequency component.

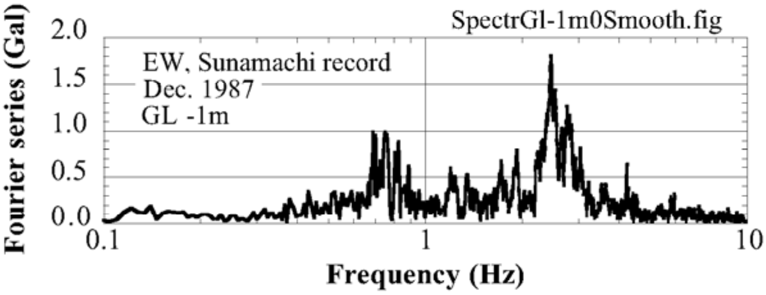

**Fig. 9.26** Fourier spectrum of Sunamachi surface acceleration record

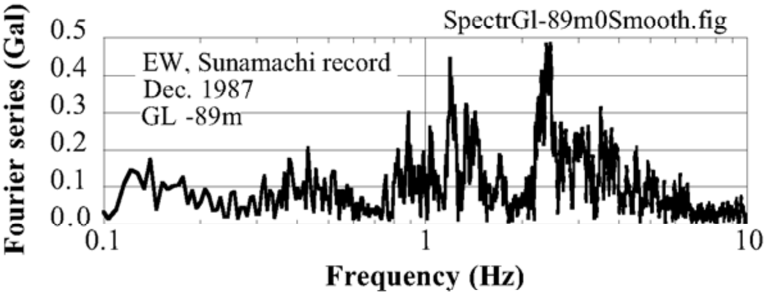

**Fig. 9.27** Fourier spectrum of Sunamachi base acceleration record

Figure 9.26 illustrates the relationship between $|C_m|$ and $m/T$, and is called the Fourier spectrum in this text. Figure 9.26 indicates that the motion is intense at the frequency of 0.8 Hz and 2.4 Hz; the former being the predominant component ,which was mentioned above. In contrast, the Fourier spectrum of the base motion (Fig. 9.27) does not have a peak spectrum value at 0.8 Hz. This implies that the alluvial soil made this frequency component stronger, which is called amplification. Note further that both spectra (Figs. 9.26 and 9.27) have peaks at 2.4 Hz. It seems therefore that this particular predominant component of acceleration was produced in the deeper deposit or the source mechanism of earthquake.

Note moreover that the strong component at around 1.3 Hz in the base motion (Fig. 9.27) disappeared in the surface motion (Fig. 9.26).

A possible draw-back of the spectra shown above is that the variation of the spectrum value fluctuates significantly, making it difficult to exactly determine the predominant frequency, frequency at which the spectrum is maximum. To solve this problem, smoothing technique was developed. Figure 9.28 demonstrates an example of smoothing in which the spectrum valued prior to smoothing is modified by

$$\text{new } S_k = 0.25S_{k-1} + 0.50S_k + 0.25S_{k+1} \qquad (9.15)$$

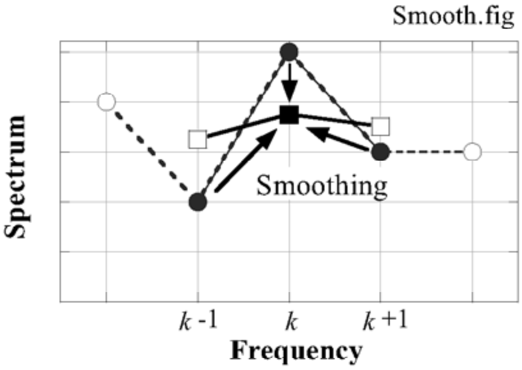

**Fig. 9.28** Example of spectrum smoothing

to be a smoothed spectrum. Equation (9.15) is called Hanning Window, and another formula of

$$\text{new } S_k = 0.23S_{k-1} + 0.54S_k + 0.23S_{k+1} \qquad (9.16)$$

is called Hamming Window. Since

0.25+0.50+0.25=1.0 and
0.23+0.54+0.23=1.0,

the use of these smoothing does not artificially reduce the energy of an acceleration record.

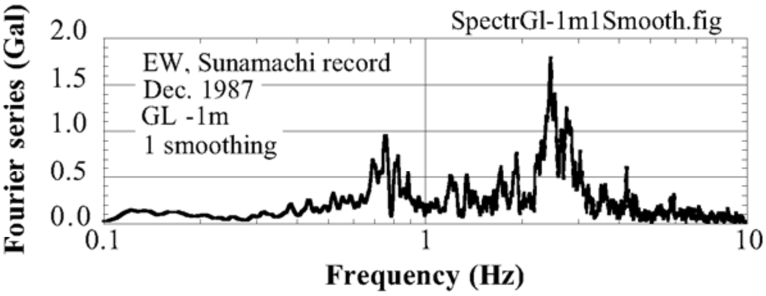

**Fig. 9.29** Fourier spectrum of Sunamachi surface motion after one time of Hanning Window

Figure 9.29 reveals the smoothing of the Sunamachi surface motion. It is found here that the spectrum still has a significant extent of fluctuation. Thus, one time of smoothing is not sufficient. Consequently, the Hanning Window was repeated up to 100 times: Figure 9.30 after 10 times of smoothing may not be sufficient. Figure 9.31 after 100 times of smoothing appears good. Thus, smoothing has to be repeated so many times until a good smoothed spectrum is obtained.

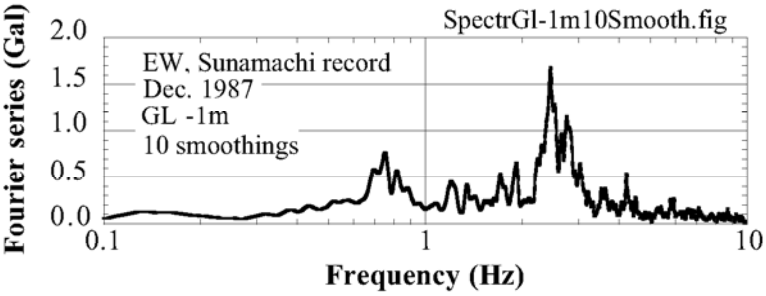

**Fig. 9.30** Fourier spectrum of Sunamachi surface motion after ten times of Hanning Window

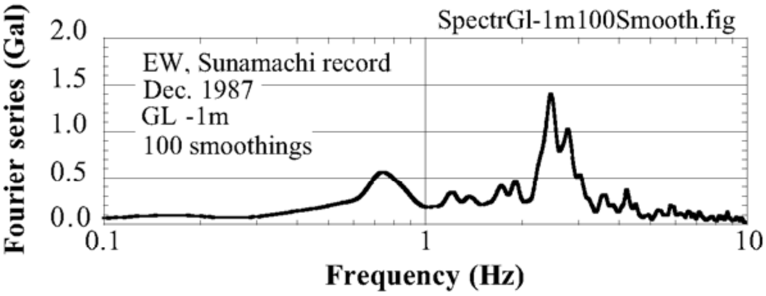

**Fig. 9.31** Fourier spectrum of Sunamachi surface motion after 100 times of Hanning Window

The amplification of motion, AMP($E$+$F$) in Sects. 6.8 and 9.6 is calculated by taking the ratio of Fourier spectra at two depths

$$\text{Amp}(E+F) = \frac{\text{Spectrum at surface}}{\text{Spectrum at base}}. \qquad (9.17)$$

It is certainly necessary to do smoothing for this ratio as well. Figure 9.32 presents the amplification thus obtained. Clearly, the amplification factor is very large at 0.8 Hz. It is reasonable, therefore, to say that the natural frequency of the Sunamachi site is 0.8 Hz and a design of a structure should avoid its natural period near 0.8 Hz in order not be troubled by resonance and significant earthquake response.

One common mistake made by unexperienced programmers in smoothing is a use of

```
S(K)=0.25*S(K–1)+0.5*S(K)+0.25*S(K+1).
```

This program changes the value of *S*(*K*) and the next step of smoothing

```
S(K+1)=0.25*S(K)+0.5*S(K+1)+0.25*S(K+2)
```

is made erroneous. One should do as what follows:

```
SK=0.25*S(K–1)+0.5*S(K)+0.25*S(K+1)
    ..................................................
SKP1=0.25*S(K)+0.5*S(K+1)+0.25*S(K+2)
S(K)=SK
SK=SKP1             (repeated for increasing K)
```

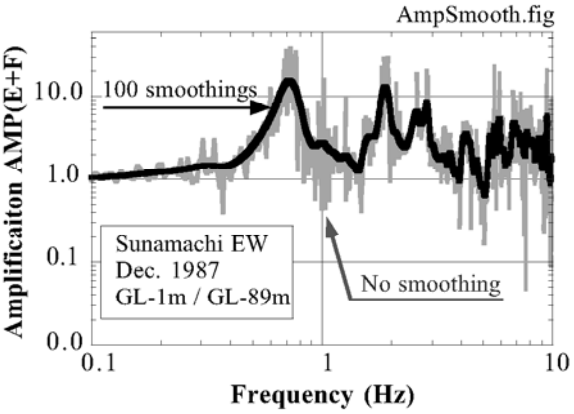

**Fig. 9.32** Amplification of motion before and after 100 times of Hanning Window

## 9.13 Dynamic Analysis with Equivalent Linear Model

In practice, the equivalent linear modeling ($G/G_{max}$ and $h$ vs. $\gamma_a$) is combined with a harmonic base motion to analyze the dynamic response of ground. Since the real base motion during earthquakes is not harmonic, its irregular time history is deconvoluted (divided) into harmonic components (Fourier series expansion), individual response to a harmonic component is calculated, and all the responses are combined to obtain the irregular response.

Since $G$ and $h$ vary with the strain amplitude, it is necessary to determine the representative strain amplitude out of an irregular time history so that strain compatible modulus and damping may be determined. Since this is possible only after analysis, the analysis has to be repeated with trials and errors on selection of strain. The flow chart is demonstrated in Fig. 9.33. A level ground with horizontal layers is assumed.

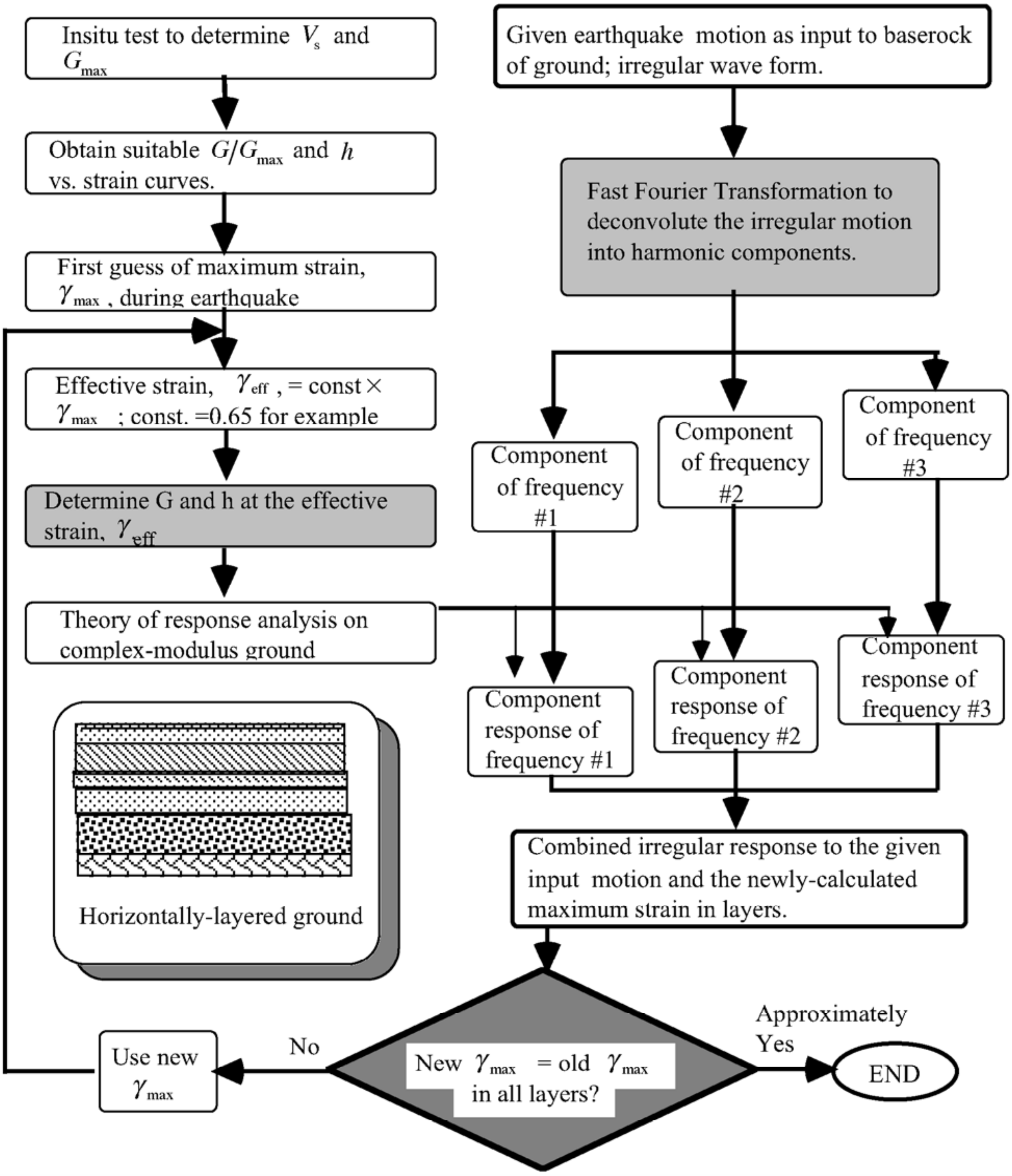

**Fig. 9.33** Flow chart of equivalent linear analysis

## 9.14 Example of Equivalent Linear Analysis

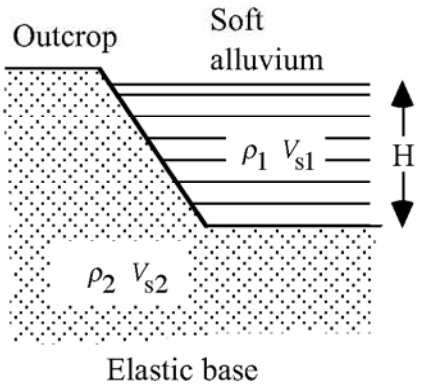

**Fig. 9.34** Model of subsoil

A brief example of an equivalent linear analysis is presented here. Figure 9.34 illustrates a model of ground that has a 7 m soft alluvium at the surface together with an elastic base. Such a field exploration as down-hole investigation has presented $V_s$ = 150 m/s in the alluvium and $V_s$ = 500 m/s in the base, respectively. Since the field exploration can generate only a small amplitude of shear strain (for example, of the order of $10^{-7}$), the dynamic analysis has to pay further attention to strain amplitude effects.

Laboratory tests on undisturbed soil specimens revealed the degradation of shear modulus and the variation of damping ratio with the amplitude of shear strain, which are illustrated by solid curves in Fig. 9.35. The modulus or $V_s$ as well as the damping ratio is modified in accordance with the estimated shear strain until a good convergence 収束 is obtained.

The present analysis assumes a harmonic shaking of 3 Hz and the outcrop amplitude of acceleration to be 4 m/s$^2$ ($2E\omega^2$ = 400 Gal in the surface deposit). Table 9.1 indicates the procedure of iteration 繰り返し計算. Note that, since the shaking is harmonic, the shear strain amplitude ($\gamma_{max}$) obtained by a previous iteration is directly used as the estimated strain ($\gamma_{eff}$) in the next iteration without multiplying by 0.65 (Sect. 9.13). The modulus and damping ratio at this strain are employed in the next dynamic analysis.

**Table 9.1** Sequence of iteration

| No. of iteration | Assumed shear strain amplitude[a] | $G/G_{max}$ | Damping ratio | Obtained surface acceleration | Obtained shear strain |
|---|---|---|---|---|---|
| 1 | $5\times10^{-6}$ : *initial guess* | 1.0000 | 0 .0200 | 4.72 m/s$^2$ | $1.59\times10^{-3}$ |
| 2 | $1.59\times10^{-3}$ | 0 .4132 | 0.1154 | 4.05 | $2.14\times10^{-3}$ |
| 3 | $2.14\times10^{-3}$ | 0.3795 | 0.1208 | 4.27 | $2.28\times10^{-3}$ |
| 4 | $2.28\times10^{-3}$ | 0.3714 | 0.1222 | 4.33 | –––––– |

a: strain at depth of $H/2$

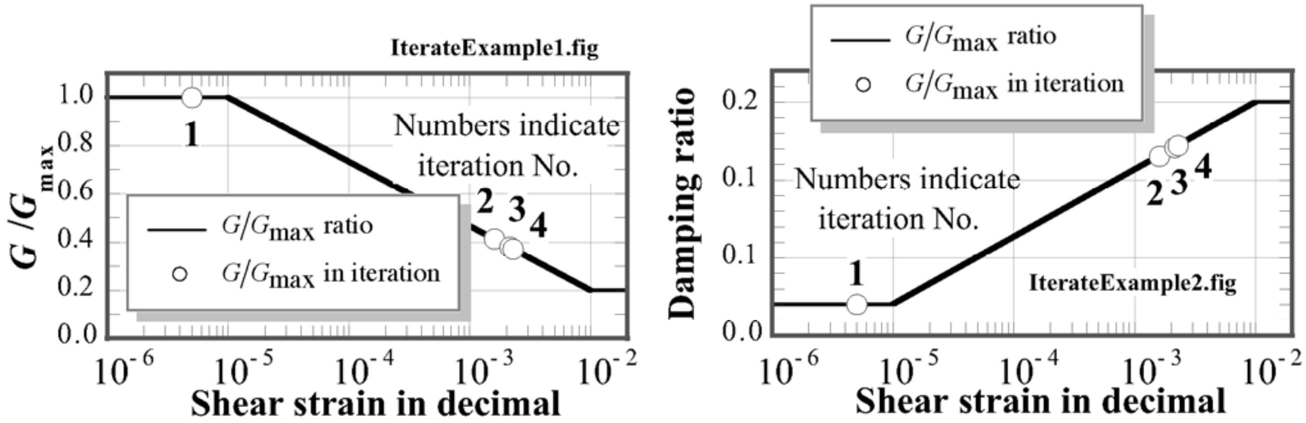

**Fig. 9.35** Variation of material properties with the progress of iteration

Since the difference between the 3rd and 4th iterations is negligible, a good convergence was obtained and the results of the 4th iteration are reported as final. Figure 9.35 indicates the variation of $G/G_{max}$ and the damping ratio with the progress of iteration.

## Exercise No. 5 Equivalent Linear Method of Analysis

The nonlinear stress–strain relationship of soils is replaced by an equivalent complex modulus model and, thereby, the equation of wave propagation is made linear. In this exercise, the soil property is specified by a hyperbolic model by Hardin and Drnevich (1972) (see Fig. 9.36) in which the skeleton curve that connects two ends of hysteresis loops is defined by

$$\tau = \frac{G_{\max}\gamma}{1+|\gamma/\gamma_r|}, \qquad (9.18)$$

where $\gamma_r$ is called the reference strain. Equation (9.18) gives the secant modulus, $G \equiv \tau/\gamma$

$$\frac{G}{G_{\max}} = \frac{\tau}{G_{\max}\gamma} = \frac{1}{1+|\gamma/\gamma_r|}. \qquad (9.19)$$

Moreover, the damping ratio, *h*, is modeled by

$$h = h_{\max}\left(1-\frac{G}{G_{\max}}\right), \qquad (9.20)$$

which fits the experimental knowledge.

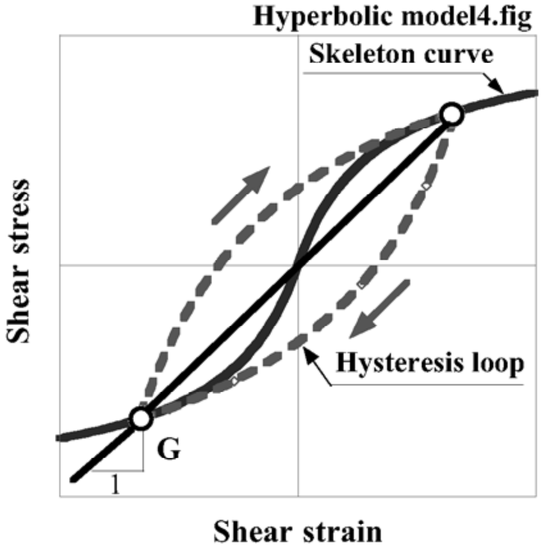

**Fig. 9.36** Model of stress–strain behaviour

Run an equivalent linear analysis on a two-layered ground in Fig. 9.37 with a harmonic outcrop motion (正弦波) of 2*E* = 0.2 m/s$^2$ and 2 m/s$^2$. The frequency is set equal to 5 Hz. The material properties are indicated in Table 9.2.

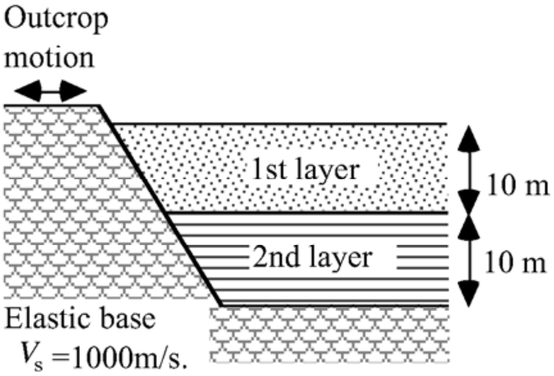

**Fig. 9.37** Soil profile

**Table 9.2** Material properties

| Layer | Mass density, $\rho$ | $V_s$ | $\gamma_r$ | $h_{\max}$ |
|---|---|---|---|---|
| 1 | 2 g/cm$^3$ | 150 m/s | $1.1\times10^{-3}$ | 0.20 |
| 2 | 2 g/cm$^3$ | 350 m/s | $3.0\times10^{-3}$ | 0.15 |
| Base | 2 g/cm$^3$ | 1,000 m/s | – – – – | 0.00 |

Summarize the procedure of trial-and-error and convergence in a table as shown below. The strain-consistent $G/G_{\max}$ and damping ratio are calculated by using $\gamma_{\text{eff}} = 1.00\times\gamma_{\max}$ at the middle depth of each layer. Do be careful of unit conversion!

To avoid common mistakes of students
1. In layer 1, $G_{\max} = 2\times150^2$ kPa.
   $\rho$ is not $2\times9.8$ but 2.
2. $E_b$ of the outcrop motion is not $2\ m/s^2$
   It is $2\div2\div\omega^2\ \ m$ because $E_b$ is the amplitude of displacement.

The answer will be as what follows; see the answer of exercises at the end of this book.

| Base acceleration | Surface acceleration | Amplification Amp(*E*+*F*) |
|---|---|---|
| 0.20 | 0.32 | 1.6 |
| 2.0 | 2.653 | 1.3 |

The amplification was made different by the nonlinear behavior of soil. The greater acceleration increased the shear strain in the soil, and reduced the shear modulus, while increasing the damping ratio. Consequently, the natural period of ground changed, and more energy was lost due to damping. Thus, the amplification during strong earthquakes is smaller than amplification during minor shaking.

Example: Outcrop motion is of 5 m/$s^2$ in amplitude and 1 Hz in frequency

| | 1st Layer | | | | 2nd layer | | | | |
|---|---|---|---|---|---|---|---|---|---|
| Iteration | Assessed strain | Shear modulus | Damping ratio | Obtained strain | Assessed strain | Shear modulus | Damping ratio | Obtained strain | Surface acc. |
| 1 | 0.0020 | 16,000 kPa | 0.129 | 0.0041 | 0.0010 | 184,000 kPa | 0.037 | 0.0010 | 6.811 |
| 2 | 0.0041 | 9,610 | 0.157 | 0.0078 | 0.0010 | 185,000 | 0.037 | 0.0010 | 8.071 |
| 3 | 0.0078 | 5,580 | 0.175 | 0.0180 | 0.0010 | 182,000 | 0.039 | 0.0013 | 11.257 |
| 4 | 0.0180 | 2,590 | 0.189 | 0.0449 | 0.0013 | 172,000 | 0.044 | 0.0010 | 13.908 |
| 5 | 0.0449 | 1,080 | 0.195 | 0.0334 | 0.0010 | 184,000 | 0.037 | 0.0002 | 5.087 |
| 6 | 0.0334 | 1,440 | 0.194 | 0.0347 | 0.0002 | 227,000 | 0.011 | 0.0002 | 6.572 |
| 7 | 0.0347 | 1,380 | 0.194 | 0.0344 | 0.0002 | 229,000 | 0.010 | 0.0002 | 6.312 |

## 9.15 Deconvolution of Earthquake Motion

The equivalent linear technique is further useful when the base incident motion has to be assessed by using the measured surface motion. This procedure is called “deconvolution.” Figure 9.38 illustrates a situation in which the surface motion at site “A” ($E_{1a}$) is known and the incident motion in the base ($E_b$) is desired. The assessed $E_b$ will later be put in at the base of another site “B” in order to calculate the surface motion ($E_{1b}$). Although $E_{1a} \neq E_{1b}$, $E_b$ at two sites are identical.

In the following example, the subsoil condition as in Table 9.3 is employed at the site A.

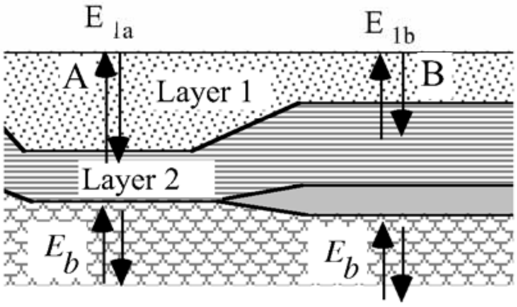

**Fig. 9.38** Deconvolution

**Table 9.3** Material properties in the example

| Layer | Thick-ness | Mass density | $V_s$ | $\gamma_r$ | $h_{max}$ |
|---|---|---|---|---|---|
| 1 | 10 m | 2 g/cm$^3$ | 150 m/s | $1.1 \times 10^{-3}$ | 0.20 |
| 2 | 10 m | 2 g/cm$^3$ | 350 m/s | $3.0 \times 10^{-3}$ | 0.15 |
| Base | | 2 g/cm$^3$ | 1,000 m/s | | 0.00 |

Assuming that the surface motion at “A” is specified by $2E_{1a}$=2.653 m/s$^2$ and 5 Hz, the deconvolution procedure of iteration is shown in what follows. Note that the solved situation at “A” is same as the one in Exercise 3 with the outcrop motion of 2 m/s$^2$. The outcrop acceleration ($2E_b$) converged to 2 m/s$^2$ as expected.

| | Layer 1 | | | | Layer 2 | | | | |
|---|---|---|---|---|---|---|---|---|---|
| Ite-ration | Estimated strain | Shear modulus ( kPa) | Damping ratio | Obtained strain | Estimated strain | Shear modulus (kPa ) | Damping ratio | Obtained strain | Surface accel. (m/s$^2$) $(2E_b)$ |
| 1 | 0.0100 | 4,460 | 0.180 | 1.02*e*-3 | 0.0050 | 91900 | 0.094 | 4.67*e*–4 | 2.431 |
| 2 | 1.02*e*–3 | 23,400 | 0.096 | 7.74*e*-4 | 4.67*e*–4 | 222000 | 0.020 | 1.05*e*–5 | 1.976 |
| 3 | 7.74*e*–4 | 26,400 | 0.083 | 7.17*e*4 | 1.05*e*–5 | 237000 | 0.005 | 7.52*e*–5 | 2.010 |
| 4 | 7.17*e*–4 | 27,200 | 0.079 | 7.03*e*-4 | 7.52*e*–5 | 239000 | 0.004 | 6.93*e*–5 | 2.002 |
| 5 | 7.03*e*–4 | 27,500 | 0.078 | 7.00*e*-4 | 6.93*e*–5 | 239000 | 0.003 | 6.79*e*–5 | 1.999 |
| end | 7.00*e*–4 | 27,500 | 0.078 | 7.00*e*-4 | 6.79*e*–5 | 240000 | 0.003 | 6.80*e*–5 | |

The second example uses $2E_{1a}$=5 m/s$^2$ and 2 Hz while making the second layer *very thin* (0.5 m thick) and *very soft* ($V_s$ = 80 m/s), while making the first layer thick (19.5 m) with $V_s$ = 150 m/s. The material properties in the second soft layer as well as the assessed outcrop motion did not converge (see Fig. 9.39). Such a problematic situation is often encountered in practice where the observed surface motion is too strong when a subsoil appears to be very soft. In reality, most probably the soft thin layer is nothing more than a local small deposit and does not extend to infinity as assumed in analysis. Such a local clay pocket should be ignored in practical analysis, although a single boring data cannot reveal its lateral size.

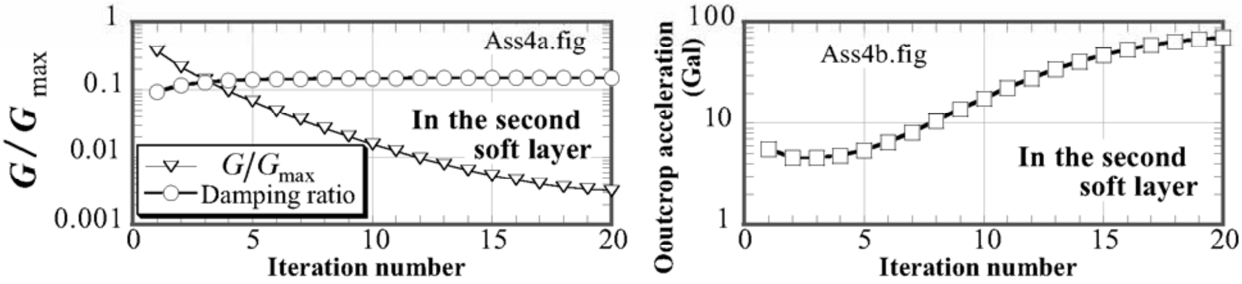

**Fig. 9.39** Example deconvolution without reaching convergence

It is meaningful to herewith introduce an example of unsuccessful deconvolution, because a similar problem is not uncommon in practice. Figure 9.40 shows the site where a deconvolution was attempted. This area was once a sea thousands of years ago when the sea level was higher than the present level. Sediments from several big rivers deposited here, and those rivers have been flooding frequently during the human period when the sea level retreated a few meters. Consequently, there remained many ponds and swamps until recent times. In the past decades, this area has been developed as a residential area.

Figure 9.41 illustrates the outside of a building where an earthquake motion was recorded. Note the differential settlement around the building due to the ongoing consolidation of the soft subsoil. Many cracks have occurred inside this building as well. The convolution of this surface motion was the aim of the analysis.

**Fig. 9.40** Soft ground condition at site of deconvolution

**Fig. 9.41** Differential settlement around building

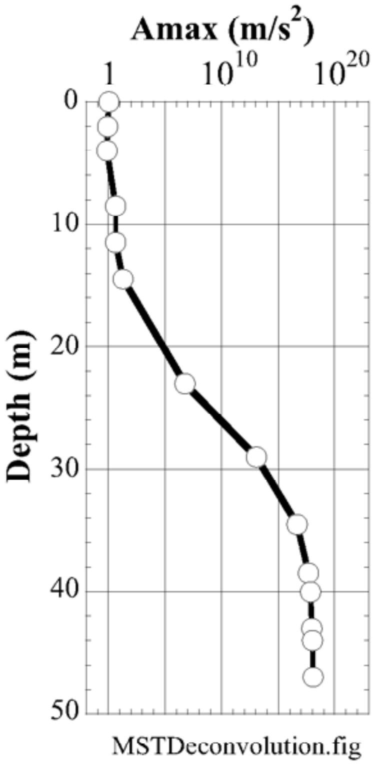

**Fig. 9.42** Poor results of deconvolution

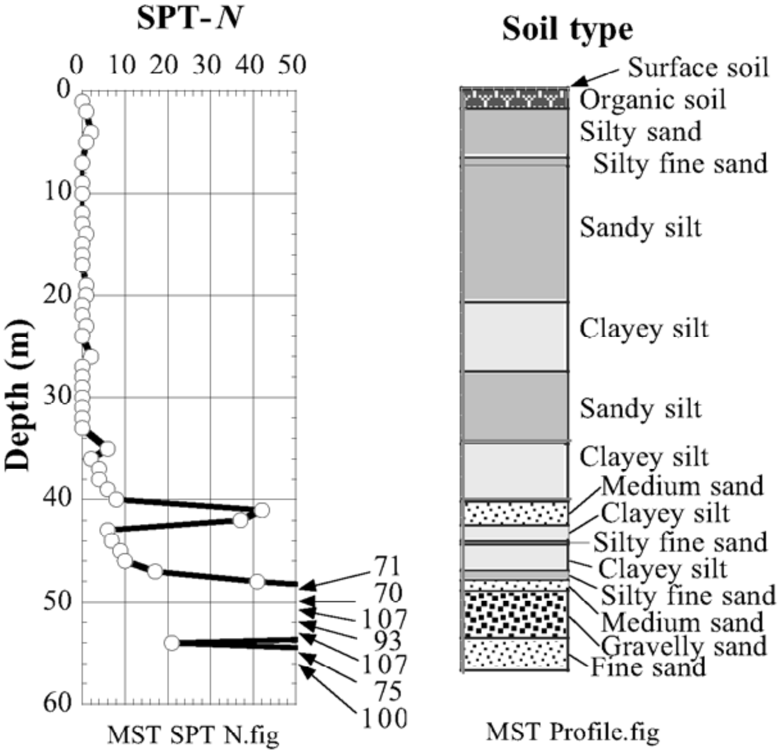

**Fig. 9.43** Soil profile at site of deconvolution

Figure 9.42 demonstrates an unsuccessful result in which the surface recorded acceleration was 1.01 m/s$^2$ while the calculated bottom motion became as large as $10^{18}$ m/s$^2$. This result is certainly nonsense. The reason for this problem lies in the extremely soft soil condition. As illustrated in Fig. 9.43, there is a very thick deposit of silty materials in which SPT-*N* value is 0 or 1. This low value of SPT-*N* made $G_{max}$ very small in the analysis (8.10), and created low $G=G_{max}(G/G_{max})$ as well. Consequently, the shear stress level in the soft subsoil was not high enough to account for the recorded acceleration of $A_{max} = 1$ m/s$^2$ in the top soil;

The equation of motion of the top soil (Fig. 9.44) states that the maximum acceleration, $A_{max}$, in the surface soil is limited by the shear strength in the subsoil, $\tau_{max}$, if the assumption of one-dimensional stratification is acceptable.

Moreover, many analyses were run on the same profile, while changing the intensity of input acceleration at the bottom. As shown in Fig. 9.45, it was not possible to reproduce the surface acceleration of 1 m/s$^2$. The reduction of acceleration above the level of 30 m below the ground surface is evident.

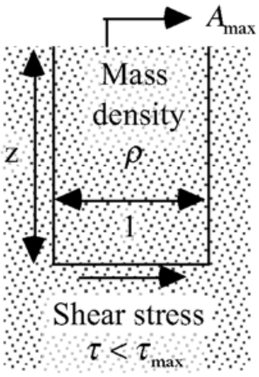

$$\rho z A_{max} = \tau \le \tau_{max}$$

**Fig. 9.44** Equation of motion for surface soil undergoing S wave propagation in vertical direction

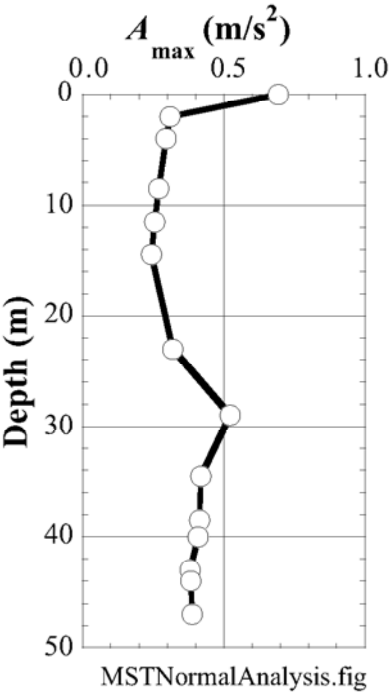

**Fig. 9.45** Normal analysis with specified acceleration amplitude at the bottom

Thus, it seems that the surface acceleration of 1 m/s$^2$ was not caused solely by the vertical propagation of S wave. Most probably, the subsoil condition was of two- or three-dimensional configuration, the seismograph in the building recorded a very local dynamic phenomenon in the building, or else. The effect of surface waves (Sects 4.7 and 4.8) is unlikely because the thick deposit of soft soil induces significant energy dissipation and would not allow the propagation of surface waves over a long distance.

## 9.16 Further Remarks on Equivalent Linear Model

- The equivalent liner model of $\tau = G(1+2ih)\gamma$ is combined with (1) the theory of wave propagation in complex-modulus media and (2) the assumption of harmonic shaking. Therefore, dividing an irregular motion into harmonic components is necessary.
- The highest frequency employed in analysis is normally 10–15 Hz. For important rigid facilities, for example, nuclear power plants, 30 Hz may be the case.
- The comparison of old and new maximum strains are made by using $G/G_{\max}$ and $h$. Those calculated by new and old maximum strains should be reasonably close to each other. When the difference is less than 1 – 5 %, the analysis is terminated (end).
- The number of iterations (trials and errors) is usually about 5–10, depending upon the required level of difference between new and old $G$ and $h$.

**Advantages of the method:**

- The equation of wave propagation is rigorously solved from the mathematical viewpoint (厳密解). Therefore, a large thickness of layers does not make a serious error in computation. Hence, the computation time can be saved by using large thickness and reduced number of layers. This is in contrast with errors in finite element method and others that are generated by unacceptably large size of layers.
- There are many experimental $G/G_{\max}$ and $h$ data in literatures. Therefore, the preparation of input data is possible without running laboratory tests.

**Disadvantages of the method:**

- In real earthquakes, $G$ and $h$ are not constant from the beginning till the end of shaking, although the method assumes that they are constant.

    Even in a single earthquake event, there is a stage in which the shaking and strain are small, whilst in other stage they are large (Fig. 9.46). Hence, it is more appropriate to use different values of $G$ and $h$ in different stages of shaking.

    Dry sand subjected to cyclic loading of constant stress amplitude increases its $G$ and decreases its h as the number of cycles increases (see Sect. 10.3).

    Loose deposit of water-saturated sand undergoing heavy shaking, which is one of the most important subject of dynamic analysis, increases the excess pore water pressure with the number of cycles. Accordingly, the effective stress decreases with time. Since $G$ of sand highly depends on the level of effective stress, *it decreases with time*. Therefore, the equivalent linear method combined with the theory of harmonic shaking should not be used on the strong earthquake response of loose sandy deposits.

        It is empirically known, however, that the method of analysis is acceptable unless a complete loss of effective stress (liquefaction) occurs.

- The effective strain is calculated by $\gamma_{\text{eff}} = 0.65 \times \gamma_{\max}$. The parameter of 0.65 is just empirical and there is no theoretical background. It is maybe related to the electric theory of AC current. When the strain time history is exactly harmonic, in contrast, the parameter should be 1.0.

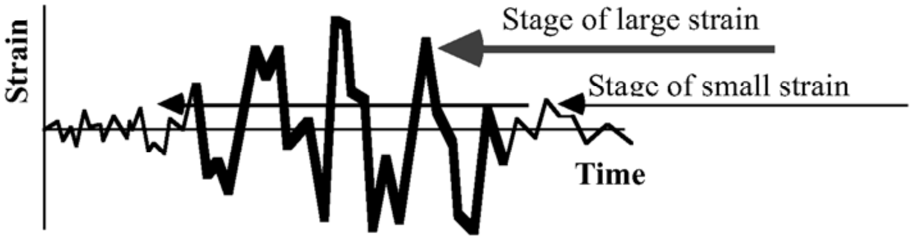

**Fig. 9.46** Conceptual time history of strain with varying magnitude

- The maximum acceleration in response is produced by harmonic components of high frequency. The strain amplitude of those components is normally small because their displacement amplitude is small, and hence large $G$ and small $h$ should be assigned to them. Since the method uses for all the frequency components common values of *G* and *h*, which are actually relevant for a larger strain amplitude, the high-frequency components are overdamped (過減衰) and the maximum acceleration is underestimated. Sugito et al. (1994) and Sugito (1995) improved this point by allocating different values of *G* and *h* to different frequency components in accordance with their respective strain amplitudes.

## List of References in Chapter 9

Hardin, B.O. and Drnevich, V.P. (1972) Shear modulus and damping in soils; design equation and curves, Proc. ASCE, Vol. 98, SM7, 667–692.

Idriss, I.M. (1990) Response of soft soil sites during earthquakes, Proc. H. Bolton Seed Memorial Symposium, pp. 273–290.

Sugito, M. (1995) Frequency dependent equivalent strain for equi-linearized technique, Proc. First Int. Conf. Earthq. Geotech. Eng., Tokyo, Vol. 2, pp. 655–660.

Sugito, M., Goda, H. and Masuda, T. (1994) Frequency dependent equi-linearized technique for seismic response analysis of multi-layered ground, Proc. JSCE, Vol. 493/III-27, pp. 49-58.

Towhata, I. (1996) Seismic wave propagation in elastic soil with continuous variation of shear modulus in the vertical direction, Soils Found., Vol. 36, No. 1, pp. 61–72.